Sedimentary Geology 440 (2022) 106240

Contents lists available at ScienceDirect

Sedimentary Geology

journal homepage: www.elsevier.com/locate/sedgeo

Unraveling overprinted formation mechanisms of massive dolostone in the Lower Triassic sequence of an isolated carbonate platform in Nanpanjiang Basin, south China

Xiaowei Li [a,*], Daniel J. Lehrmann [b], John Luczaj [c], Brian M. Kelley [d], Dave L. Cantrell [a,e], Meiyi Yu [f], Nathaniel Ledbetter Ferrill [b], Jonathan L. Payne [a]

[a] Department of Geological Sciences, Stanford University, Stanford, CA 94305, USA
[b] Department of Geosciences, Trinity University, San Antonio, TX 78212, USA
[c] Department of Natural & Applied Sciences, University of Wisconsin-Green Bay, Green Bay, WI 54311, USA
[d] Department of Geosciences, The Pennsylvania State University, University Park, PA 16802, USA
[e] Cantrell GeoLogic, Franklin, TN 37069, USA
[f] Department of Resources & Environmental Engineering, Guizhou University, Guiyang, Guizhou Province 550025, China

ARTICLE INFO

Article history:
Received 31 May 2022
Received in revised form 21 August 2022
Accepted 23 August 2022
Available online 27 August 2022

Editor: Dr. Moretti Massimo

Keywords:
Dolomitization
Reflux
Burial
Carbonate platform
Early Triassic

ABSTRACT

Massive dolomitization is common in carbonate platforms but determining the causes of dolomitization remains challenging. A particular difficulty lies in identifying cases where petrographic and geochemical attributes of dolostone related to one mechanism could be obscured by a later, different one. To better understand whether traditional approaches are sufficient to unravel the origins of dolostone resulting from successive, different mechanisms, this study investigates the formation mechanism(s) of dolostone along a platform-to-basin transect of a Permian-Triassic isolated platform in the Nanpanjiang Basin. The dolostone in the Lower Triassic succession comprises three dolomite phases that can be distinguished through field relationships, petrography, $^{87}Sr/^{86}Sr$ ratios, and microthermometry. Dolomite type 1 formed due to the reflux of platform-top evaporated seawater that flowed through the platform interior in the Early Triassic. Dolomite types 2 and 3 are interpreted to have formed at elevated temperatures during or after Late Triassic platform burial and to have played a secondary role in forming the dolostone. The dolomitizing fluids that resulted in the formation of dolomite types 2 and 3 were derived from Early Triassic seawater-like fluid that was expelled from the Lower Triassic basinal carbonate sediments and moved updip to the platform interior. Dolomitized clasts in partially or non-dolomitized slope breccias demonstrate pre-burial timing of dolomite type 1, and distinguish the earlier dolomitization from later, post-burial dolomitization represented by dolomite types 2 and 3. Dolomite type 1 retains its Early Triassic seawater $\delta^{13}C$ and $^{87}Sr/^{86}Sr$ signatures, whereas overlapping geochemical fields of the three types of dolomite (trace element concentration, $\delta^{18}O$) imply that burial dolomitizing fluids locally reset the geochemistry of dolomite type 1. This finding suggests that the same dolomite archive may retain well-preserved or altered data depending on the specific geochemical proxy and that identifying individual dolomitization mechanisms using geochemical proxies is possible only in some cases.

1. Introduction

Mechanisms of dolomite formation have been studied for more than a century because dolomitized strata have enormous economic value where they host abundant hydrocarbons or ore deposits (Al-Awwad and Collins, 2013; Davies and Smith Jr, 2006; Jiang et al., 2014). Despite this long history of study, dolomite formation remains a topic of active inquiry, in part because dolomitization is difficult to replicate in the laboratory under ambient conditions (Land, 1998). Various models for the formation of platform-scale massive dolostone have been proposed, among which the seepage-reflux (Adams and Rhodes, 1960; Dravis and Wanless, 2018), geothermal convection (Dong et al., 2020; Whitaker et al., 1994; Whitaker and Xiao, 2010), burial compaction (Barnaby and Read, 1992; Machel and Anderson, 1989), and fault-controlled hydrothermal dolomitization models (Hendry et al., 2015; Koeshidayatullah et al., 2020) are the most prominent.

If massive dolostone formed through the sequential action of multiple processes related to different mechanisms (i.e., two or more mechanisms), the prediction of porosity, permeability, and other properties of the dolomite body is challenging because the processes are not simply additive (Garaguly et al., 2018; Haas et al., 2014; Nader et al.,

* Corresponding author.
E-mail address: geo.xwli@gmail.com (X. Li).

https://doi.org/10.1016/j.sedgeo.2022.106240
0037-0738/

2004; Ronchi et al., 2011; Wang et al., 2015). Furthermore, geochemical proxy data often allow non-exclusive interpretations of chemistry and temperature of dolomitizing fluids as well as conditions of depositional and diagenetic environments (Machel, 2004). A key question for determining whether subsequent dolomitization mechanisms can be distinguished from early ones within a given partially dolomitized body is whether evidence of early-formed dolomite related to different mechanisms is still detectable by conventional approaches or if, instead, novel methods must be applied.

In order to advance our understanding of massive dolostone and its formation, it is necessary to first determine how signatures of dolomitization processes are currently preserved, especially when these occurred through two or more different mechanisms. Determining the process of dolomitization in ancient carbonate platforms is important because it can be used to reveal fluid chemistry, fluid-flow pathways, and development of pore systems (Koeshidayatullah et al., 2020; Machel, 2004; Saller, 2004).

Carbonate platforms in the Nanpanjiang Basin of south China, including the attached Yangtze Platform and several isolated carbonate platforms (Figs. 1 and 2), are ideal for studying dolomitization through two or more mechanisms. The platforms are well exposed along several intact platform-to-basin transects (Enos et al., 2006; Lehrmann et al., 1998; Minzoni et al., 2014). Lower Triassic strata of the Yangtze Platform, the Great Bank of Guizhou (GBG), and the Chongzuo-Pingguo Platform are partially dolomitized (Enos et al., 2006; Kelley et al., 2020; Lehrmann et al., 2007; Minzoni et al., 2014; Shultz et al., 2013), yielding a basin-wide distribution of massive dolostone (Fig. 2C). Investigating the dolomitization mechanism(s) responsible for the massive dolostone body across diverse depositional environments of the GBG builds a foundation towards assessing global, regional, and local controls on the basin-wide distribution of the massive dolostone. Because the Lower Triassic platform margin of the GBG is largely composed of dolomitized oolitic shoals (e.g., Rongling section in Fig. 4), the results of this study may be particularly relevant to dolomitized reservoir facies in the Feixianguan Formation in the Sichuan Basin of China and the Khuff and Dalan formations in the Middle East (Amel et al., 2015; Ehrenberg et al., 2007; Jiang et al., 2018).

The GBG has an advantage over the targets of previous case studies where dolomite bodies are attributable to multiple episodes of dolomitization likely related to different mechanisms (Garaguly et al., 2018; Nader et al., 2004; Wang et al., 2015). This is because a partially dolomitized interval is preserved and the growth history of the GBG is exceptionally well-constrained through a 2-D transect from the platform interior to slope facies (Figs. 3 and 4; Lehrmann et al., 1998, 2020; Kelley et al., 2020). Moreover, the partially dolomitized succession is advantageous because it preserves multiple stages of dolomitization that clearly relate to different mechanisms in different depositional environments, such as dolomitized caps of peritidal facies in the platform interior and dolomitization fronts at the margin and slope. The transect along the Bianyang syncline (Fig. 3) exposes the distribution and field relationships of the dolostone and it enables detailed petrography across multiple depositional environments for assessing flow direction and constraining relative timing of dolomitization in adjunction with conventional geochemical analyses. Documenting the petrographic and geochemical attributes of limestone and dolostone across different depositional environments would further complement dolomitization models and improve prediction of dolostone properties where outcrops are not accessible or limited core samples are available for analyzing subsurface analogs.

To better understand how overlapping dolomitization mechanisms are preserved, this study (1) documents field relations, cross-cutting relationships, petrographic textures, and geochemical composition of massive dolostone from the GBG, (2) determines the overall context of diagenetic alteration, (3) evaluates the origins of massive dolostone, and (4) investigates the chemistry, temperature, and source(s) of dolomitizing fluids.

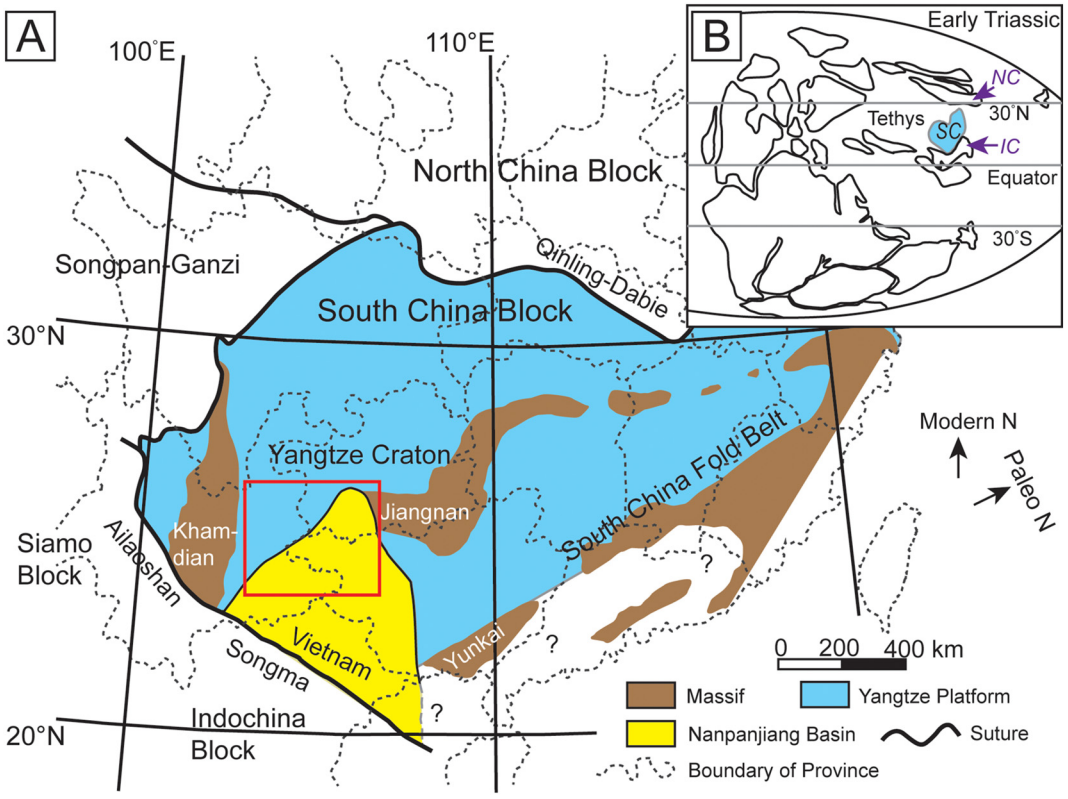

Fig. 1. Geologic setting. (A) Present locations of the Yangtze Platform and Nanpanjiang Basin. Red box denotes the extent of the Nanpanjiang Basin shown in Fig. 2A. Modified after Minzoni et al. (2014). (B) Global plate reconstruction and locations of the South China Block (SC), the North China Block (NC), and the IndoChina Block (IC) in the Early Triassic.

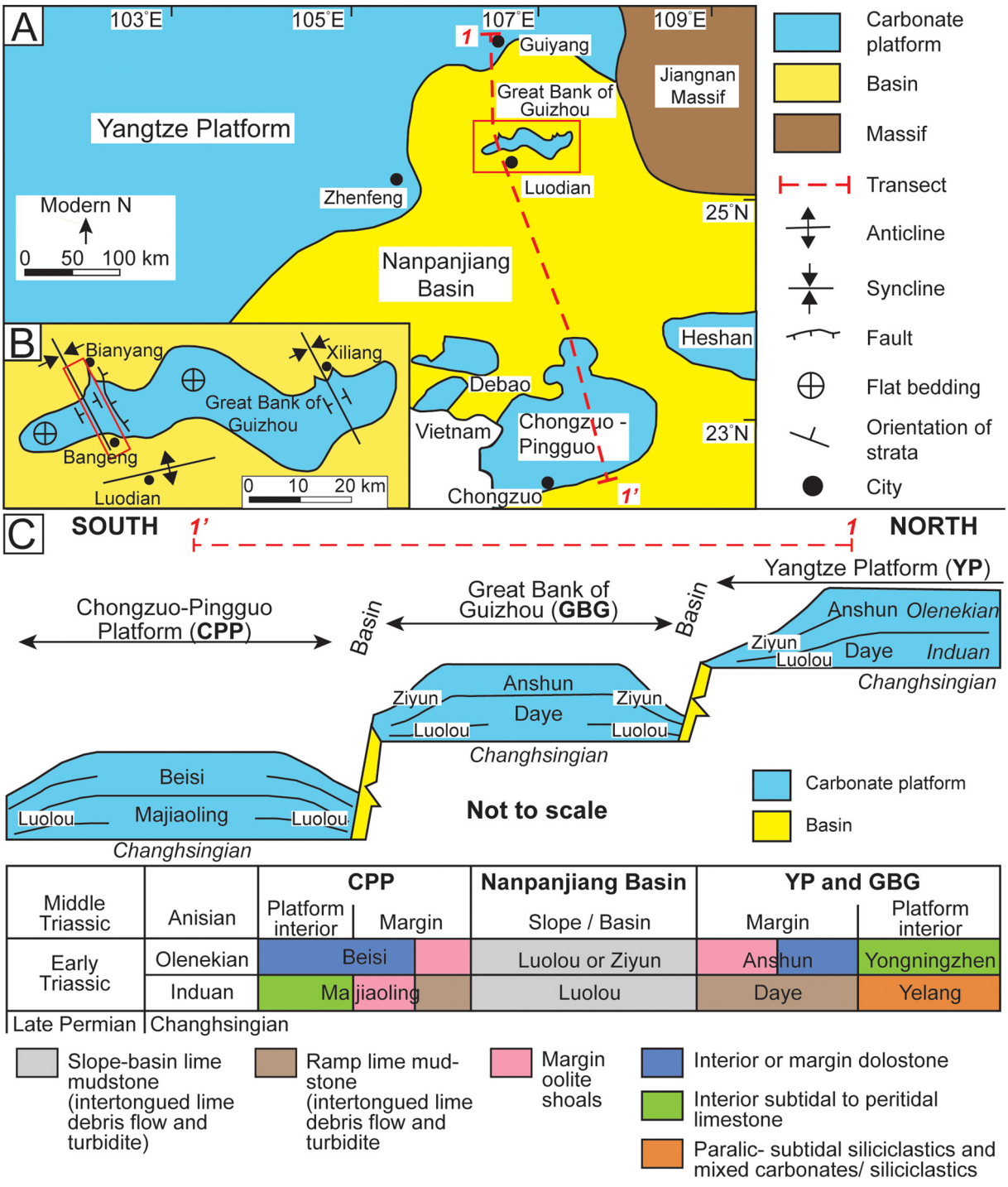

Fig. 2. Detailed view of the Nanpanjiang Basin and the Great Bank Guizhou (GBG). (A) Position of the GBG is indicated by a red box. Schematic stratigraphic framework along the red dashed line (1-1′) is shown in panel (C). (B) Detailed view of the GBG with the Bianyang syncline (faulted syncline). The red box in (B) denotes the studied transect of the GBG whose satellite image and stratigraphic architecture are shown in Fig. 3. There are no dolomitized strata between the fault and the studied transect. (C) Simplified Early Triassic stratigraphic framework of the Nanpanjiang Basin, Yangtze Platform, GBG, and Chongzuo-Pingguo Platform. A dolomitized stratigraphic interval of the Lower Triassic (Anshun and Beisi Formation) shows a basin-wide distribution of massive dolostone. Modified after Minzoni et al. (2014). (For interpretation of the references to colour in this figure legend, the reader is referred to the web version of this article.)

2. Geologic setting

The South China Block, comprising the Yangtze Craton and the South China Fold Belt, was located in tropical eastern Tethys during the latest Permian and Triassic (Fig. 1). The Nanpanjiang Basin formed an embayment to the southern margin of the Yangtze Platform (present coordinates; Figs. 1 and 2). There are several Permian to Triassic isolated carbonate platforms in the Nanpanjiang Basin (Fig. 2A). The GBG is dissected by a N-S-trending syncline (Bianyang syncline in Fig. 2B) that exposes a continuous 2-D platform-to-basin cross-section of the stratigraphic architecture (Fig. 3). Strata of the cross-section along the Bianyang syncline dip at roughly 65° to the southwest (Fig. 3A).

The GBG exhibits substantial spatial and temporal variations in stratigraphic architecture (Kelley et al., 2020; Lehrmann et al., 2020, 1998; Li et al., 2012). It began as a gently dipping ramp during the earliest Triassic but soon evolved to become a high-relief, steep-sloped carbonate

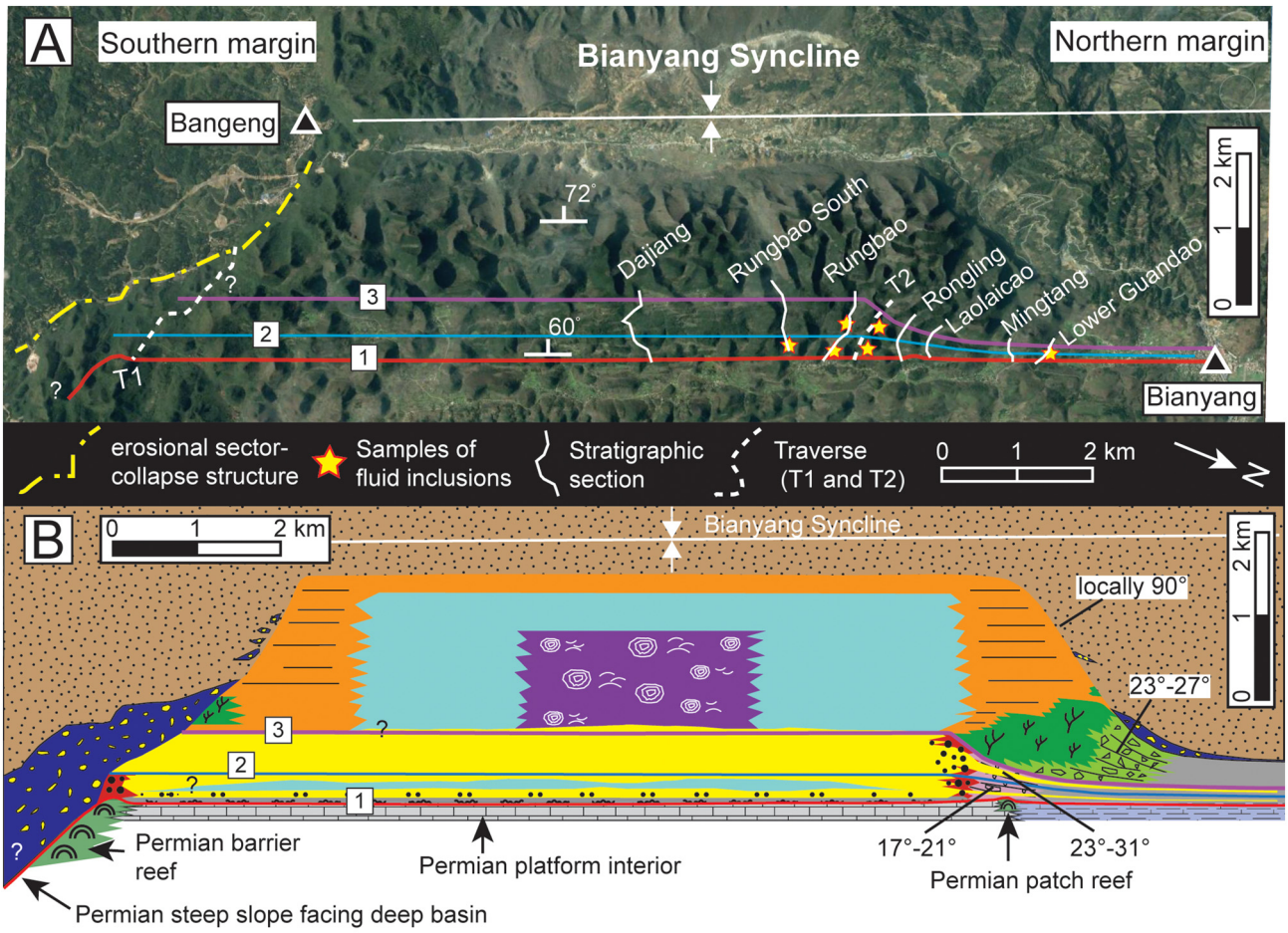

Epoch	Age	Platform interior	Platform margin	Slope-basin
Middle to Late Triassic	Anisian to Carnian	Skeletal-peloidal packstone; Peritidal limestone; Molluscan-oncolitic packstone	Skeletal-peloidal packstone; *Tubiphytes* boundstone	Siliciclastic turbidite; Collapse carbonate breccia; *Tubiphytes* boundstone; Lime mudstone, grainstone, breccia; *Tubiphytes* boundstone derived breccia
3				
Early Triassic Focus of this study	Olenekian	Anshun Fm.: Dolostone	Anshun Fm.: Dolostone; Oolite; Dolo-oolite	Luolou Fm.: Breccia containing clasts of oolite; Lime mudstone (intertonged carbonate debris and turbidites); Dolostone
2				
	Induan	Daye Fm.: Peritidal limestone; Lime mudstone; Dolostone; Microbialite; Dolo-oolite	Daye Fm.: Dolostone; Oolite; Dolo-oolite	Luolou Fm.: Breccia containing clasts of oolite; Lime mudstone (intertonged carbonate debris and turbidites); Dolostone
1				
Late Permian	Changhsingian	Fossiliferous packstone and grainstone	Sponge-microbial boundstone	Siliceous lime mudstone

Fig. 3. Satellite image and stratigraphic architecture of the GBG along the Bianyang syncline. (A) Satellite image of the GBG by courtesy of Google Earth. (B) Stratigraphic architecture and principle lithofacies of the GBG through time. Detailed lithofacies, grain/fossil types, and spatial thickness variation of the massive dolostone are referred to Fig. 4. The architecture of the northern margin comes from Lehrmann et al. (1998) and Kelley et al. (2020). The architecture within the platform interior is from Lehrmann et al. (1998). The southern margin architecture derives from Lehrmann et al. (2020). (For interpretation of the references to colour in this figure legend, the reader is referred to the web version of this article.)

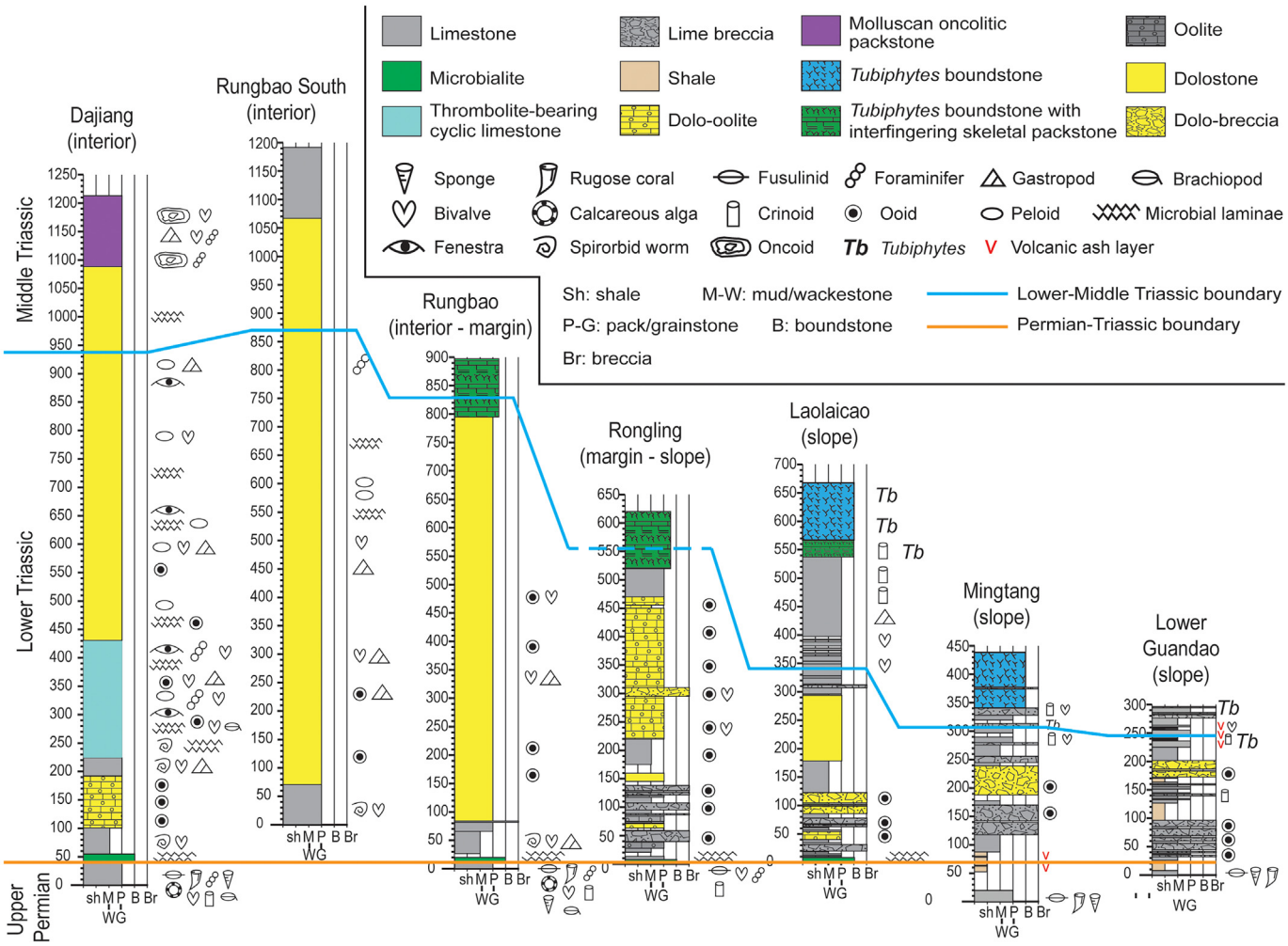

Fig. 4. Correlation of measured stratigraphic sections across the platform-to-basin transition based on carbon isotope chemostratigraphy (blue line) modified from Lehrmann et al. (2015) and Kelley et al. (2020). Locations of the stratigraphic sections are shown in Fig. 3A. (For interpretation of the references to colour in this figure legend, the reader is referred to the web version of this article.)

platform with oolitic shoals, skeletal fragments, and peloids at its margins during the later Induan and Olenekian (Fig. 3B; Kelley et al., 2020; Li et al., 2021). During Anisian time, it generally maintained a high-relief platform with a prograding *Tubiphytes* reef growing on the platform margin and slope (Fig. 3B; Lehrmann et al., 1998; Kelley et al., 2020). It then developed a bypass escarpment in the late Anisian to Ladinian before its drowning and burial by siliciclastic turbidites in the early Carnian. Detailed descriptions of depositional facies and platform architecture are presented by Lehrmann et al. (1998, 2007, 2020) and Kelley et al. (2020); herein, the focus is on the dolomitized Lower Triassic strata.

Facies of Induan age in the platform interior grade upward from basal microbial boundstone to thin-bedded lime mudstone and dolomitized oolite, followed by peritidal facies (Fig. 3 and Dajiang section in Fig. 4). The peritidal facies consists of meter-scale cycles with bases of skeletal packstone, oolitic packstone, and cyanobacterial boundstone (stromatolite and thrombolite) and caps of laminated mudstone to packstone (Lehrmann et al., 1998). Marginal shoal facies comprise oolitic grainstone with subordinate molluscan packstone (Li et al., 2020; Rongling section in Fig. 4). Coeval slope facies are composed of shale, clast- and mud-supported lime breccia, calcareous turbidites, and periplatform lime mudstone (e.g., Laolaicao and Mingtang sections in Fig. 4; Lehrmann et al., 1998; Kelley et al., 2020). Carbonate grainstone and mud- or clast-supported breccia were primarily derived from aggradational oolitic shoals at the platform margin in which partial to pervasive dolomitization occurred (Fig. 3B and Rongling section in Fig. 4).

Continued aggradation of the margin during the Olenekian generated a high-relief, steep-sloped carbonate platform (Fig. 3B; Kelley et al., 2020). Ooid grains, skeletal fragments, and peloids continued to dominate at the platform margin, whereas peritidal limestone formed in the platform interior and later underwent dolomitization. The dolomitized peritidal limestone is composed of meter-scale, shallowing-upward cycles with bases of burrowed molluscan-peloidal packstone and domal stromatolite and caps of fenestral laminite (Lehrmann et al., 1998). Clast-supported breccias in the slope, mainly comprising clasts of the margin-derived oolite and subordinate slope-sourced lime mudstone, are commonly dolomitized in the northern slope (e.g., Mingtang and Lower Guandao sections in Fig. 4; Kelley et al., 2020). The southern margin near Bangeng collapsed in the Middle Triassic and clasts derived from the Early Triassic margin and interior were transported to the basin (Lehrmann et al., 2020).

3. Methods

Two hundred and eighty-nine samples were collected from seven stratigraphic sections and from two traverses in the platform interior, margin, and slope facies of the GBG (Fig. 3A). Cross-cutting relationships between dolostone, host limestone, and other diagenetic features, as well as locations of dolomitized clasts, were observed to help determine

relative timing of formation of dolostone and migration direction of dolomitizing fluids.

One hundred and seventeen standard blue-dyed, epoxy-impregnated petrographic thin sections were stained with Alizarin Red S and analyzed by LEICA DM 2700P optical microscope to distinguish dolomite from calcite, document pore types, crystal sizes, geometries, and relative timing of dolomitization to other diagenetic events. Seventeen polished rock slabs from the platform margin and slope facies were used to identify macroscopic petrographic features of dolomite and compare isotopic measurements of dolostone to adjacent host limestone. Twelve samples collected from the platform interior to basin margin were observed by a Cold-cathode Relion III CL luminescence microscope with a beam voltage of 15 kV, a current of 0.5–1 μA, and a beam diameter of 2 mm in order to identify stages of dolomite crystal growth.

Double-polished wafers ~100 μm thick were prepared from nine samples. Fluid inclusions were analyzed at Trinity University and the University of Wisconsin-Green Bay to check the replicability of measured data using standard methods described in Goldstein and Reynolds (1994). In dolomite, fluid inclusion assemblages (FIAs) were defined as populations of two-phase aqueous fluid inclusions present in either the inclusion-rich crystal cores or those aligned parallel to growth zonation of dolomite crystals. Inclusions were measured for homogenization temperature (T_h) without pressure correction and ice final melting temperature (T_m) using a Leica DM 2500 petrographic microscope with a Linkam THM600/TS90 heating and cooling stage at Trinity University and a Nikon Optiphot petrographic microscope with a Fluid Inc.-adapted USGS design gas-flow heating and freezing stage at the University of Wisconsin-Green Bay. These measurements were used to determine the formation temperature of dolomite and salinity of the dolomitizing fluids. The stages were calibrated through synthetic fluid inclusions between −120 °C to 400 °C. T_h and T_m are measured and reported with a precision of 0.5 °C and 0.1 °C, respectively. T_m of fluid inclusions in dolomite were further converted to salinity following Bodnar (1993).

For carbon and oxygen isotopic analysis, powders of dolomite or calcite from 141 rock samples were collected by a 0.3 mm diameter dentist's drill after identifying the area of study interest on fresh polished surfaces through a binocular microscope to avoid contamination. Powders of host limestone and its nearby dolostone (all <5 cm apart) were also selected for comparative analysis in samples that were not pervasively dolomitized. Fifty to 100 μg of dolomite or limestone powders were then reacted with anhydrous phosphoric acid for 24 h to release CO_2. The collected CO_2 was then analyzed by a Finnigan MAT251 mass spectrometer calibrated with NBS-18 standard at Stanford University. Isotope ratios are reported in parts per thousand relative to the Vienna Peedee Belemnite (VPDB) standard. Analytical precision is better than 0.05 ‰ for $\delta^{13}C$ and 0.06 ‰ for $\delta^{18}O$, respectively.

For strontium isotopic analysis, powders of dolomite or calcite from 26 rock samples were collected by a 0.3 mm diameter dentist's drill after identifying the area of study interest. Carbonate digestion and Sr separation were performed in the Stanford ICPMS/TIMS Facility Class 100 Clean Lab. High purity (Fisher Optima) 7 N nitric acid was used to fully dissolve carbonate samples, and Sr was isolated from the sample solution using Eichrom Sr ion exchange resin. Total procedural blanks for carbonate dissolution and separation ranged from 100 pg to 1 ng ($n = 6$) and are considered negligible as they represent <0.2 % of the total mass of Sr per analysis. Purified Sr samples were analyzed for $^{87}Sr/^{86}Sr$ using the Nu Plasma HR MC-ICPMS. Samples were run in dry plasma mode in a 100 ppb Sr, 2 % nitric acid solution using a Nu DSN-100 Desolvation Nebulizer System for sample introduction. Masses 83 and 85 were monitored for Kr and Rb interferences, respectively, and were corrected using the iterative approach of Jackson and Hart (2006). Data were corrected for instrumental mass fractionation using the sample-standard-bracketing technique with SRM-987 ($^{87}Sr/^{86}Sr = 0.710248$) as the bracketing standard. Daily reproducibility is determined by the 2σ value of the standard for the day (0.000035 to 0.000078) and was typically better than the long-term reproducibility. Samples that were analyzed when daily reproducibility was worse than the long-term average were re-analyzed in another session and an error-weighted average value is reported. Long-term reproducibility is determined through the repeated measurement of the Stanford in-house carbonate sample PGDR1. Data collected during the time frame of this study yielded $^{87}Sr/^{86}Sr = 0.709907 \pm 46$ (2σ; $n = 10$).

To further decipher the origin(s) of dolomite crystals, the JEOL JXA-8230 electron microprobe at Stanford University was used to measure elemental compositions (Sr, Fe, and Mn) of 34 dolostone and limestone samples. The electron microprobe is equipped with X-ray spectrometers and a backscattered electron detector. Operation conditions of the electron microprobe during measurement were set to be 15 kV accelerating voltage and 10 nA beam current with diameter of 5 to 10 μm. Count times were 60 s on peaks, and 30 s on each background. Dolomite and calcite standards were used for calibration.

4. Results

4.1. Field relationships

Massive dolostone is generally laterally continuous within the Lower Triassic platform interior. Cumulative thickness of dolomitized intervals thins basinward, decreasing from approximately 700 m in the platform interior (Dajiang section) to 40 m in the slope facies (Lower Guandao section in Fig. 4).

Dolomitization is often pervasive and fabric retentive to fabric destructive in the platform interior regardless of the original limestone lithofacies (Fig. 5A and B). The original texture of dolomitized oolite is sometimes apparent on weathered surfaces (Fig. 5C). Surface weathering of the dolomitized peritidal facies reveals depositional textures and lithofacies, such as lime mudstone with horizontal lamination (Fig. 5A), peloidal packstone (Fig. 5D), and fenestral limestone (Fig. 5E). Local outcrops of the peritidal limestone are cross-cut by fractures along which dolomitization occurred (Fig. 5F).

The coeval platform margin is mainly composed of medium-bedded to massive oolite with subordinate mollusk packstone (Fig. 6A to C). Although the platform margin facies is usually pervasively dolomitized, sedimentary structures such as parallel and wavy laminations and foresets of oolitic dunes are preserved (Fig. 6A and D). In partially dolomitized intervals of oolite, dolomitization cross-cuts bedding planes or occurs selectively along bedding planes (Fig. 6E and F). The extent of dolomitization sometimes co-varies with depositional texture within a single bed of oolite. Oolitic grainstone not composed of composite coated grains usually experienced pervasive dolomitization (Fig. 6A), whereas oolitic grainstone including composite coated grains sometimes exhibits fabric-selective dolomitization in which individual ooids are preferentially dolomitized, occurring adjacent to early marine fibrous calcite cements (Fig. 6G). Coarsely crystalline calcite cements occasionally infill vugs and fractures in dolostone (Fig. 6H).

Dolomitization in slope deposits at the northern margin is usually pervasive, with dolomite selectively replacing clast- or mud-supported breccia rather than lime pack- or grainstone and periplatform lime mudstone intervals (slope sections in Fig. 4 and Fig. 7A to C). Clast- and mud-supported breccia at the southern margin (traverse 1 in Fig. 3A), which did not undergo pervasive dolomitization, contains lime mud and dolomitized clasts of microbialite (Fig. 7D), oolite (Fig. 7E), fenestral limestone, and mudstone (Fig. 7F). Clasts of dolomitized fenestral laminite are cross-cut by fractures along which light tan, fine- to medium-crystalline dolomite halos are developed at an outcrop of the southern margin (Fig. 7F and G). A similar habit occurs along fractures in the lime mudstone and mollusk packstone facies at the upper slope near Rongling section of the northern margin (Fig. 7H). Dolomitization is most pervasive in the extensively fractured

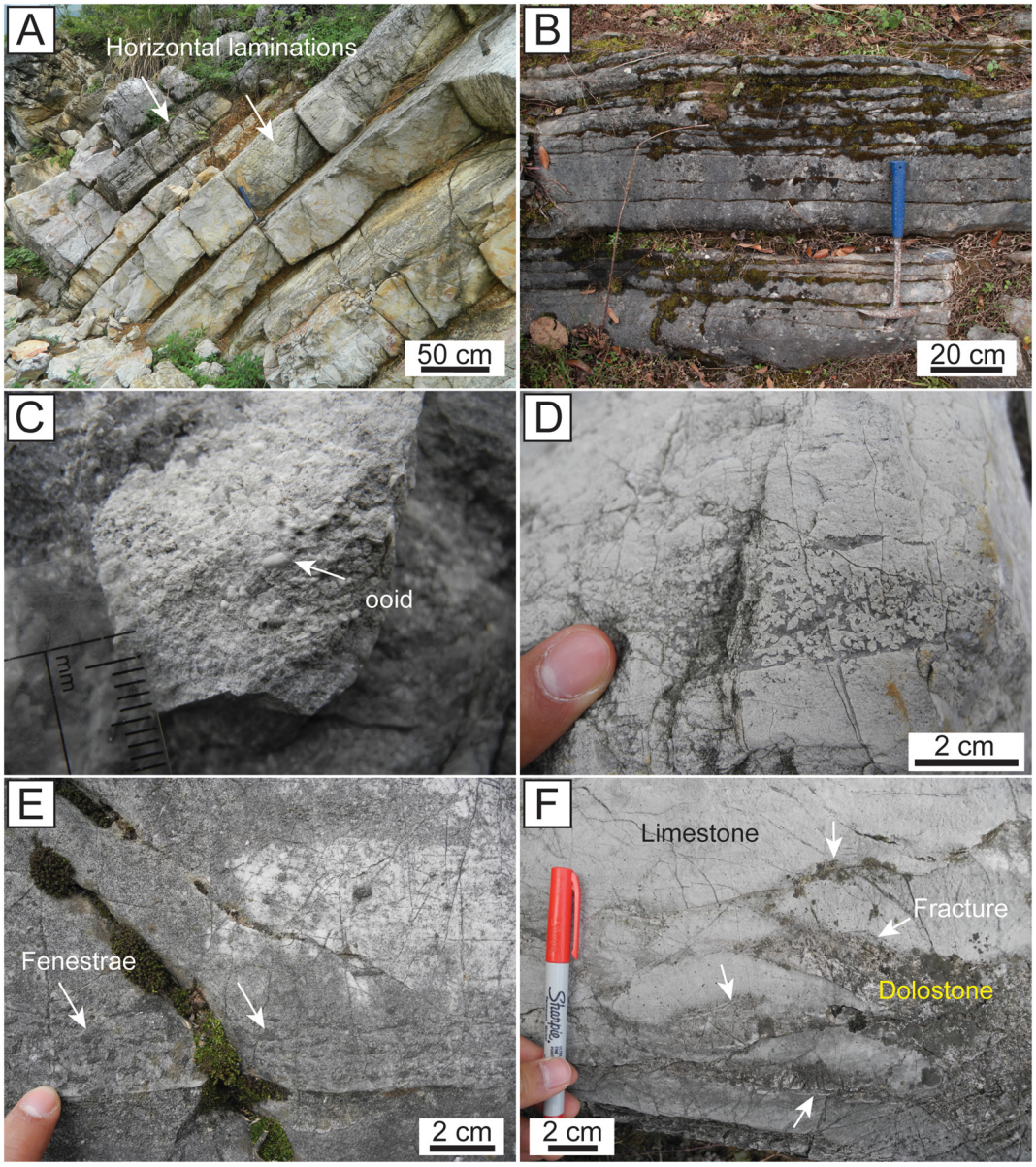

Fig. 5. Outcrop features of massive dolostone in the platform interior. (A) Medium to thick bedded dolostone with horizontal laminations from traverse 1 near Bangeng. (B) Thin bedded dolostone at Rungbao South section. (C) Pervasively dolomitized oolitic grainstone at Dajiang section. (D) Massive dolostone locally displays the original texture of peloidal packstone from traverse 1 near Bangeng. (E) Massive dolostone locally showing fenestrae at Dajiang Section. (F) Light gray limestone in the platform interior is fractured and dark gray dolomitization preferentially develops along the fractures near Rungbao South section.

area and its intensity wanes away from the fractures as indicated by its fading tan halo (Fig. 7H).

4.2. Petrographic and cathodoluminescence analysis

4.2.1. Calcite type 1 and 2

Calcite type 1 (C1), with crystals range from 20 to 1500 μm in length, is usually present as isopachous fibrous cements that fill primary interparticle porosity (Fig. 8A). Calcite type 2 (C2), with crystals ranging from 40 to 200 μm across, occurs in clear drusy to blocky cements occluding primary interparticle, fenestral, shelter, and moldic porosity (e.g., Fig. 8B), and sometimes engulfs concavo-convex grain contacts (Fig. 8B).

4.2.2. Calcite type 3

Calcite type 3 (C3), which is characterized by clear subhedral to blocky crystals ranging from 300 μm to 1 cm across, occasionally replaces dolomite cement (Fig. 8C) and infills intercrystalline pores and vugs in dolomitized oolite (Fig. 8D), oolitic molds (Fig. 8E), mollusk molds (Fig. 8F), and fractures (Figs. 8G). C3 ranges from non-luminescent to brightly luminescent (Fig. 8H).

4.2.3. Dolomite type 1

Dolomite type 1 (D1, Table 1) has various crystal sizes (~5 to 250 μm across) and geometries (anhedral to subhedral). Although lime micrite is replaced by microcrystalline dolomicrite (D1; Dolostone textures defined by crystal size is referred to Chatalov (2013)) in some slope deposits (lime mud- and wackestone) and on the platform top (muddy sediments in lagoon and tidal flat environments), the original textures are usually recognizable in thin section (Fig. 9). Dolomicrite (D1) in the platform interior consists of fine (<20 μm) crystals displaying dull-red luminescence (Fig. 9A and B). Gypsum crystals, ~100 to 400 μm long, are only preserved with dolomicrite and dolomitized microbial laminae on the platform top (Fig. 9A and C). Peloidal packstone and

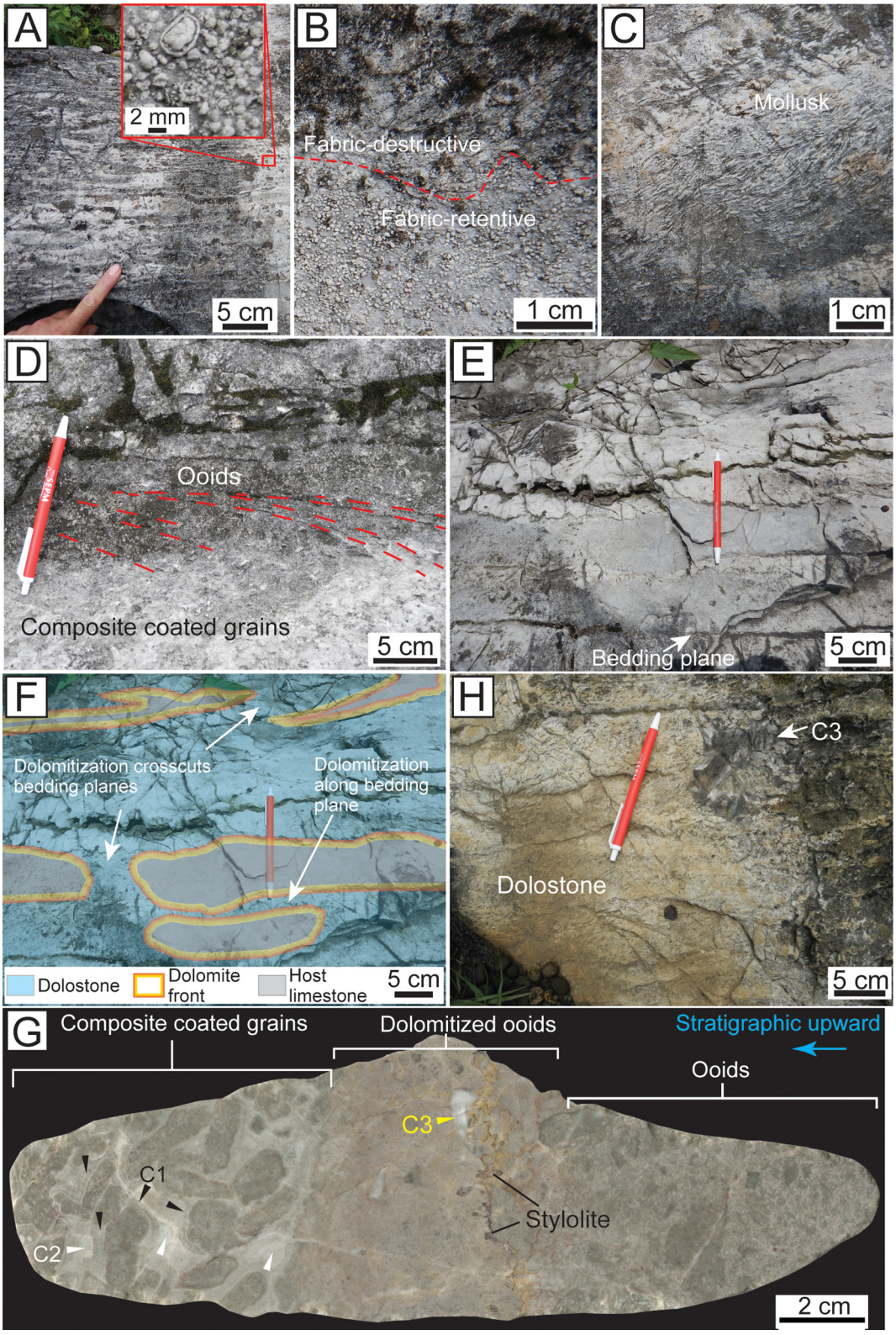

Fig. 6. Outcrop features of massive dolostone at the platform margin. (A) Dolomitized oolite with wavy laminations at Rongling section. (B) Pervasively dolomitized oolite showing fabric-destructive and fabric-retentive features within the same bed. (C) Dolomitized mollusk packstone at Rongling section. (D) Variations of sedimentary structures in dolo-oolite at Rongling section. Composite coated grains in the lower portion, foresets of dunes partition (red dashed curves) in the middle, and parallel laminations (ooids) in the upper portion (also see panel G). (E) Dolomitization cross-cuts bedding planes at Rongling section. Dolomitization preferentially occurs along bedding planes and halo of dolostone wanes from the bedding planes to the interior of a bed. (F) Same panel (E) with annotation. (G) A polished slab collected nearby panel (D) from Rongling section showing partially dolomitized oolite. Isopachous calcite type 1 (C1) and blocky calcite type 2 (C2) fills the interparticle pores between the composite coated grains. Calcite type 3 (C3) formed at a later stage. Dolomite type 1 (dolo-ooids) is cross-cut by stylolite. (H) Massive dolostone is cross-cut by fractures and coarsely crystalline calcite type 3 (C3) infills the fractures and vugs at Rongling section. (For interpretation of the references to colour in this figure legend, the reader is referred to the web version of this article.)

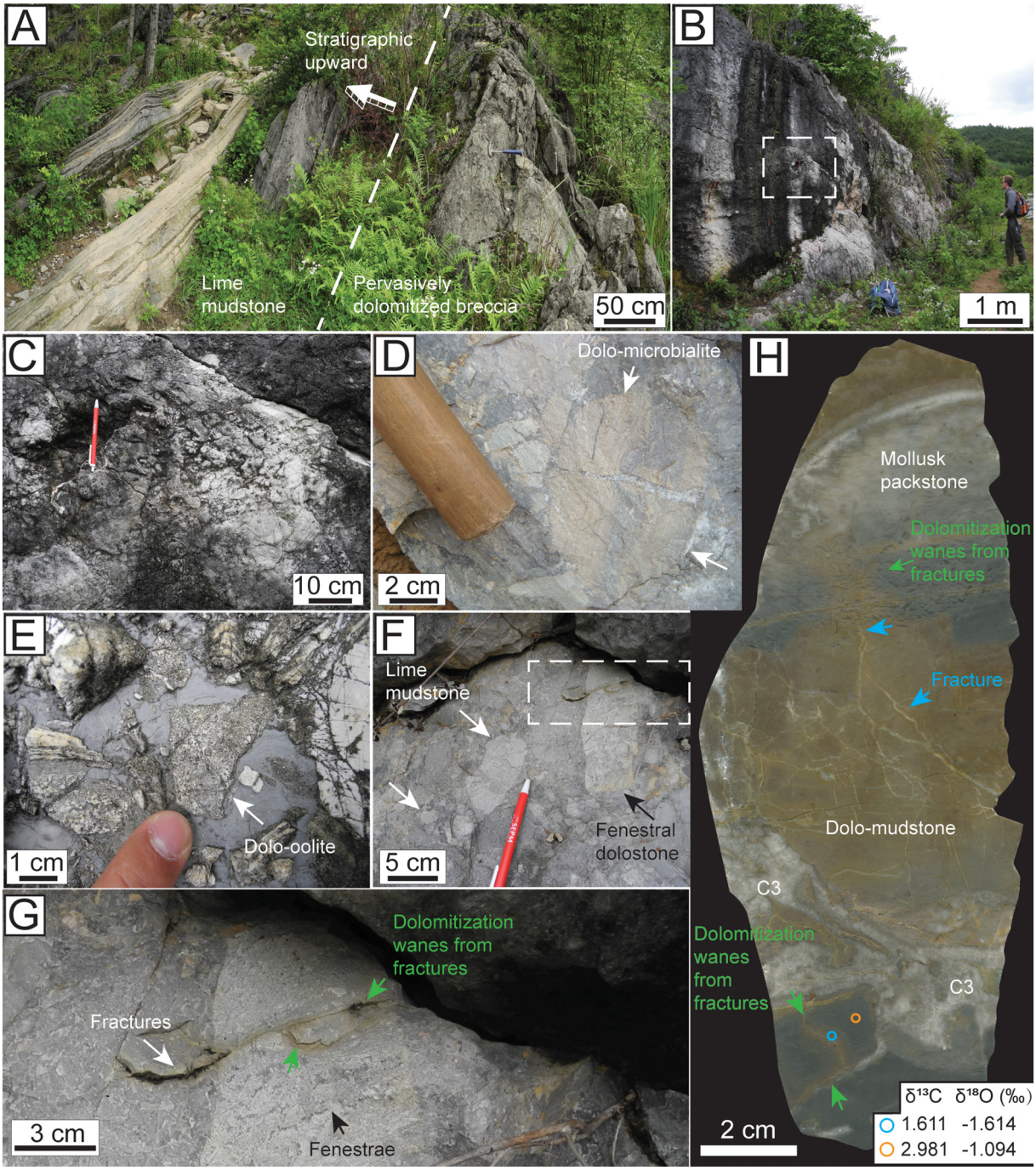

Fig. 7. Outcrop features of massive dolostone at the slope. (A) Dolomitization preferentially occurs in slope clast-supported breccia and thin-bedded lime mudstone is usually undolomitized at Rongling section. (B) Pervasively dolomitized slope clast-supported lime breccia near Mingtang section. Details of the outcrop in the dashed box are displayed in panel (C). (D) Clast-supported slope breccia contains light tan dolomitized clasts of microbialite from traverse 1 near Bangeng. (E) Slope breccia contains clasts of dolomitized oolite from traverse 1 near Bangeng, whereas the gray micrite is undolomitized. (F) Slope clast-supported breccia contains clasts of lime mudstone and dolomitized fenestral limestone from traverse 1 near Bangeng. Outcrop details in the box are shown in panel (G). (G) Dolomitized fenestral laminated clast is cross-cut by fractures along which dolomitization of a later stage occurred. Medium-crystalline tannish dolomitization halo wanes from the fracture. (H) Partially dolomitized limestone is cross-cut by fractures at Rongling section (sample no. RL-469.2). Dolomitization of a later stage preferentially occurs along fractures and light tan dolomitization halo wanes from fractures. Fracture-related pores are filled by calcite type 3 (C3). Dolomite along fractures (blue circle) has a lighter value of $\delta^{18}O$ than its adjacent lime mudstone (orange circle). (For interpretation of the references to colour in this figure legend, the reader is referred to the web version of this article.)

microbial laminae in the platform interior are typically replaced by D1 that exhibits a dull-red cathodoluminescence (Fig. 9D to G).

At the platform margin, if the host oolite is not pervasively dolomitized, a dolomitization manner is present where D1 preferentially replaced generations of calcite cements (C1) that surround ooids (Fig. 10A), the margins of ooids (Fig. 10B), and the cores of ooids (Fig. 10C to E), causing an irregular outline of ooids (Fig. 10B). At the slope, the re-transported dolomitized clasts of oolite show the same dolomitization manner (Fig. 10F) and clasts of dolomicrite (D1) sitting within lime mud are also present (Fig. 10G).

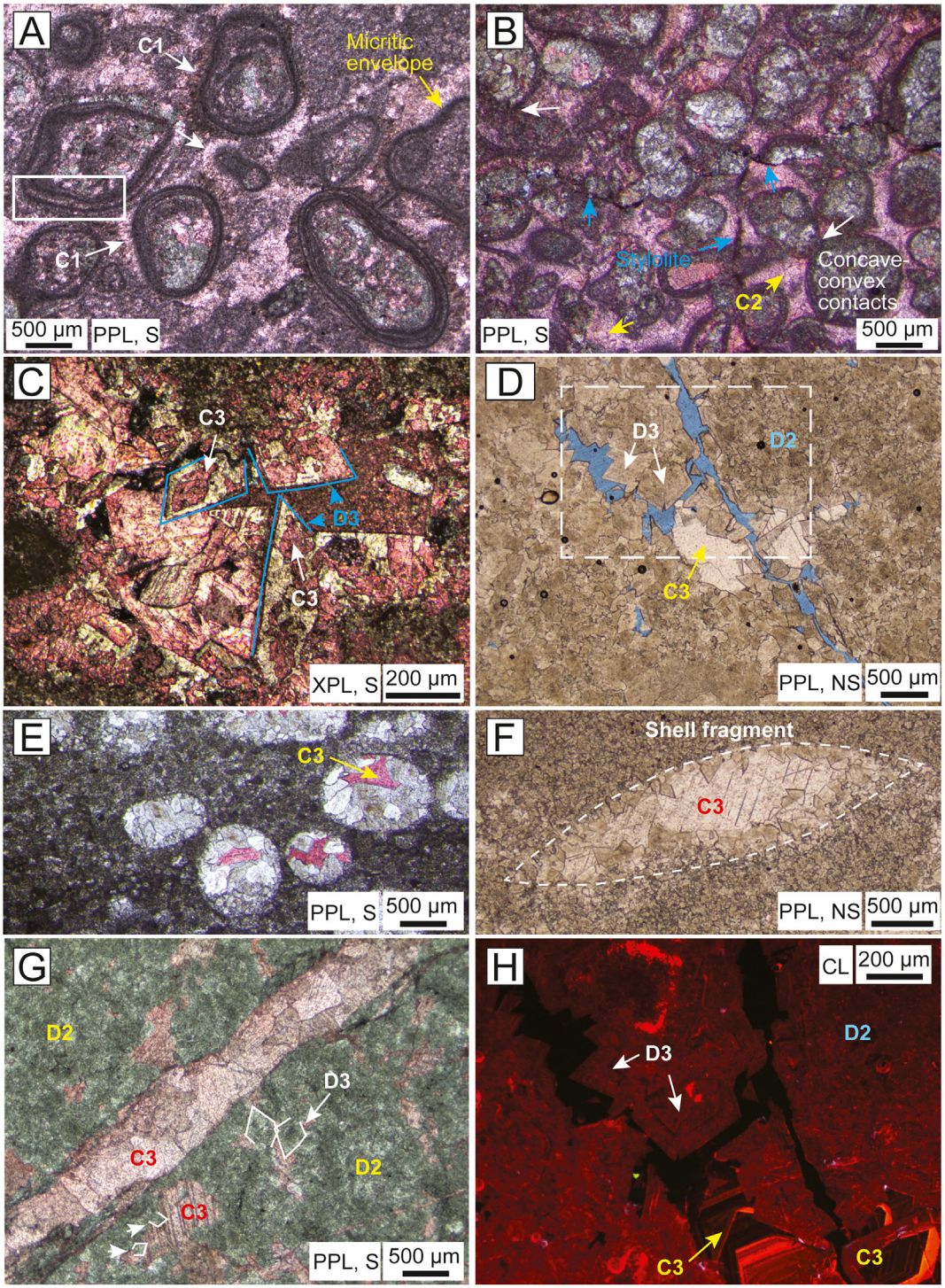

Fig. 8. Photomicrographs of calcite type 1 (C1), calcite type 2 (C2), and calcite type 3 (C3). (A) Isopachous C1 fills interparticle pores among ooids at the platform margin. Micritic envelope helps preserve the outline of ooids after neomorphism and dolomitization. Triassic ooids are interpreted to be bimineralic due to high-Mg calcitic micritic cortical laminae alternating with coarser layers of brickwork structure inferred to result from recrystallization of tangential aragonite (shown in the white rectangle). (B) Replacive dolomite preferentially replaces ooids rather than C2 at the platform margin. C2 could engulf the concave-convex contacts between ooids. (C) Dolomite rhombohedrons are partially leached and replaced by calcite (C3) within fractures in slope breccia (traverse 1). (D) Blocky C3 fills vuggy and intercrystalline space in dolomitized oolite at the platform margin. CL image of the area in the rectangle is shown in panel (H). (E) C3 is developed in oolitic molds from the platform interior. (F) C3 is developed in the central cavity of dissolved shells. (G) Blocky C3 fills a fracture at the platform margin. Euhedral D3 and anhedral D2 are adjacent to the fracture. S = stained with Alizarin Red S; NS = non-stained; PPL = plane polarized light; XPL = cross polarized light; CL = cathodoluminescence light. (For interpretation of the references to colour in this figure legend, the reader is referred to the web version of this article.)

4.2.4. Dolomite type 2

Dolomite type 2 (D2, Table 1) has various crystal sizes (~5 to 300 μm long) and geometries (anhedral to subhedral). It has a relatively broader range of crystal sizes than D1 (~5 to 250 μm; Fig. 11A to C). D2 replaces oolite at the platform margin and in the platform interior (i.e., the oolitic grainstone interval above the thin bedded lime mudstone at Dajiang section in Fig. 4) with both showing similar features in cathodoluminescence where the

Table 1
Observation of three types of dolomite and interpretation of their formation mechanisms.

Types of dolomite	Field observation	Petrographic observation	Fluid inclusion observation	Geochemical observation	Interpreted origin and temperature of dolomitizing fluids	Interpreted mechanism of dolomitization, flow pathway, timing, and volume of dolostone
Dolomite type 1 (D1)	(1) Cumulative thickness thins towards basin margin (From ~650 m at Dajiang section in the interior to ~250 m at Rongling section at the margin in Fig. 4); (2) Dolomitized clasts of microbialite, oolite, fenestral limestone are in slope lime breccia where matrix is undolomitized (Fig. 7D to G)	(1) 5 to 250 μm across, anhedral to subhedral; (2) Co-present with evaporite (gypsum in the platform interior (Fig. 9A & C)); (3) Dolomitized clasts of lime mudstone, oolite, and fenestral limestone in slope lime breccia (Fig. 10F & G); (4) Dull-red luminescence (Fig. 9B & E)	Single-phase fluid inclusions within clasts of dolomitized oolite in slope lime breccia	(1) $^{87}Sr/^{86}Sr$ of D1 are within the range of Early Triassic seawater (Fig. 17)	(1) Early Triassic evaporated seawater on the platform top that was significantly <50 °C (consistent with single-phase fluid inclusions; Goldstein and Reynolds, 1994)	(1) Reflux dolomitization during the Early Triassic (Fig. 19B); (2) Dolomitized clasts and undolomitized lime micrite suggests dolomitization occurred in near-surface or shallow burial environment in the Early Triassic (Fig. 19B) before resultant dolomitized facies were eroded and then transported to the basin due to margin collapse in the Middle Triassic (Fig. 19C); (3) D1 in the platform interior has greater volume than D2 and D3
Dolomite type 2 (D2)	(1) Dolomitization is developed along fractures in platform interior (Fig. 5F), margin (7H), and slope (Fig. 7G); (2) Dolomitization (D2) preferentially follows slope lime breccia rather than grainstone and mudstone (see slope dolostone in Figs. 4 & 7A); (3) Cumulative thickness of slope dolostone is ~40 m thick (Fig. 4); (4) Dolomitization front points to the platform interior; (5) Crystal size is generally coarser at the basin than the platform interior	(1) ~5 to 300 μm across, anhedral to subhedral; (2) Dull luminescence and clotted texture (Fig. 11B & E)	(1) All two-phase fluid inclusions (Fig. 13E); (2) High Th (81.2 to 175 °C; Fig. 13H); (3) High salinity (Fig. 13I)	(1) $^{87}Sr/^{86}Sr$ of D2 is mainly within the range of the Early Triassic seawater with two exceptions (Fig. 17); (2) D2 along fractures has a lighter $\delta^{18}O$ value than adjacent host limestone (Fig. 7H)	(1) Fluid of modified Early Triassic seawater origin trapped in the Lower Triassic basinal carbonate sediments in deep burial environment; (2) The fluid likely incorporated radiogenic Sr from siliciclastic sediments of the Jiangnan Massif (Fig. 17) during migration	(1) Burial dolomitization happened during or later than the Late Triassic Carnian (Fig. 19D); (2) Fluid migrated from the Lower Triassic basinal carbonate sediments (dolostone mainly composed D2 and D3 in the slope and basin margin is ~40 m thick; Fig. 4) updip to the platform margin and interior along fractures and permeable strata (Fig. 19D); (3) Volume of D2 and D3 is smaller than D1
Dolomite type 3 (D3)	Usually being present with D2	(1) Subhedral to euhedral, limpid, 80 to 500 μm across; (2) alternating dull to bright red luminescence (Fig. 11B)	(1) All two-phase fluid inclusions; (2) High Th (113.4 to 237.1 °C; Fig. 13H); (3) Mostly high salinity (Fig. 13I)	$^{87}Sr/^{86}Sr$ of D3 is within the range of the Early Triassic seawater (Fig. 17)	Similar to D2	Similar to D2

ooid core has dull luminescence and clotted texture (Fig. 11A and B). Mollusk packstone at the platform margin usually exhibits pervasive dolomitization in thin section (Fig. 11D). D2 replaced precursor calcite cements between mollusk shells, displaying dull red luminescence with bright patches (Fig. 11E). D2 also co-occurs with dolomite type 3 (see below) along fractures in the platform interior and margin (e.g., Fig. 7H).

4.2.5. Dolomite type 3

Dolomite type 3 (D3, Table 1) occurs in subhedral to euhedral, limpid cements ranging from 80 to 500 μm (Fig. 11A). The growth bands of D3 are characterized by alternating dull to bright red luminescence adjacent to D2 (Fig. 11B). It occurs within interparticle pores (Fig. 11A), intercrystalline and vuggy pores (Fig. 11C), mollusk molds (Fig. 11D and E), oolitic molds (Fig. 11F), and fractures (Fig. 11G). D3 could be present together with 5 to 300 μm-long, anhedral to subhedral D2 (Fig. 11G and H). Some D3 crystals display curving outlines and undulatory extinction (Fig. 11I and J). D3 with undulatory extinction are developed at the platform interior, platform margin, slope, and basin margin. D3 crystals, attached to the walls of fractures, are partially replaced by C3 (Fig. 8C; see Section Calcite type 3 above). The partially leached and calcitized dolomite rhombohedrons are very rare (i.e., only present in one thin section) and only occur within fractures in slope facies (Fig. 8C).

4.2.6. Other non-carbonate diagenetic phases

In addition to the calcite and dolomite diagenetic phases described above, non-luminescent chert cements exhibiting undulating extinction are rarely developed in local fractures of dolomitized slope sediments (i.e., only recognized in one thin section; Fig. 12). Pyrite crystals, ~5 to 60 μm across, are preserved in multiple depositional environments spanning from the shallow platform top to the deep basin margin and are most common in platform-top micritic facies (Fig. 9A).

4.2.7. Spatial variation trend of preserved porosity

Very low preserved porosity (<1 %) is identified from thin sections of dolostone collected from the platform interior of the GBG. The low porosity is preserved in fractures and vugs in dolomitized oolite and

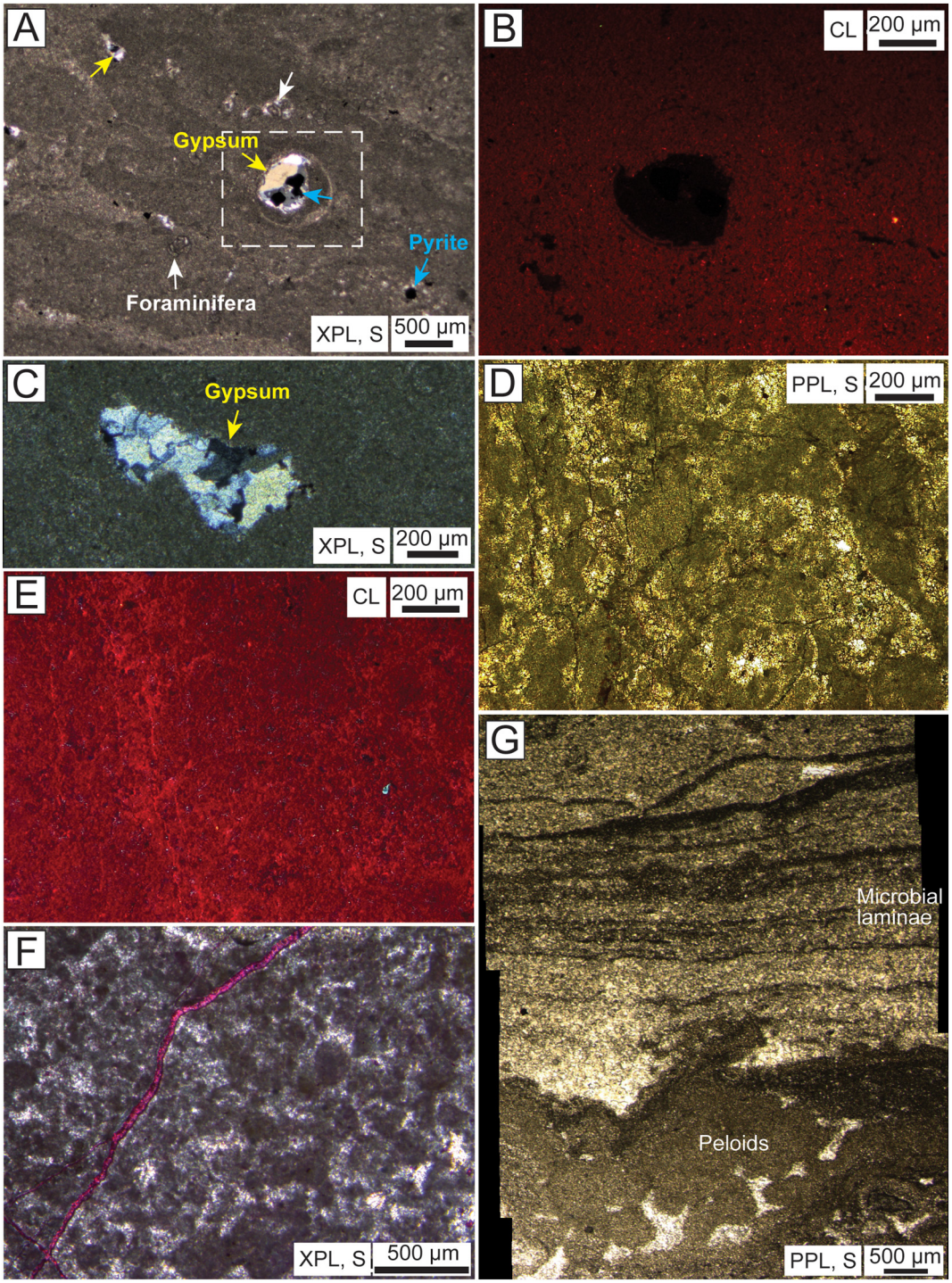

Fig. 9. Photomicrographs of dolomite type 1 (D1) in the platform interior. (A) Fine- to medium-crystalline gypsum, fine-crystalline pyrite, and foraminifera are present in dolomitized micritc limestone of the platform interior (Dajiang section). (B) CL image of the area in the dashed box of panel (A). (C) Gypsum in dolomitized lime mudstone from Dajiang section. (D) Dolomitized peloidal packstone from Dajiang section. (E) CL image of panel (D). (F) Dolomitized peloidal packstone is cross-cut by a later calcite vein. (G) Dolomitized microbial laminae and peloidal packstone from Dajiang section. S = stained with Alizarin Red S; PPL = plane polarized light; XPL = cross polarized light; CL = cathodoluminescence light. (For interpretation of the references to colour in this figure legend, the reader is referred to the web version of this article.)

peloidal packstone. Similarly, preserved porosity is also very low (<1 % in fractures) in dolomitized breccia, dolomitized lime packstone, and dolomitized micrite within the slope. In contrast, preserved porosity (predominantly vugs, fractures, and intercrystalline pores) in dolomitized oolite and peloidal packstone (Fig. 11A and C) in dolostone samples collected from the platform margin has relatively greater values with a range of 1 % to 6 % and an average value of 3 %.

4.3. Fluid inclusion petrography and microthermometry

Nine wafers were prepared and examined to determine the petrography of fluid inclusions. Six of them (see sample locations in Fig. 3A) with the best fluid inclusion petrographic relationships were selected for heating and freezing measurement of fluid inclusions. D1 crystals that are large enough for observation only include single phase aqueous

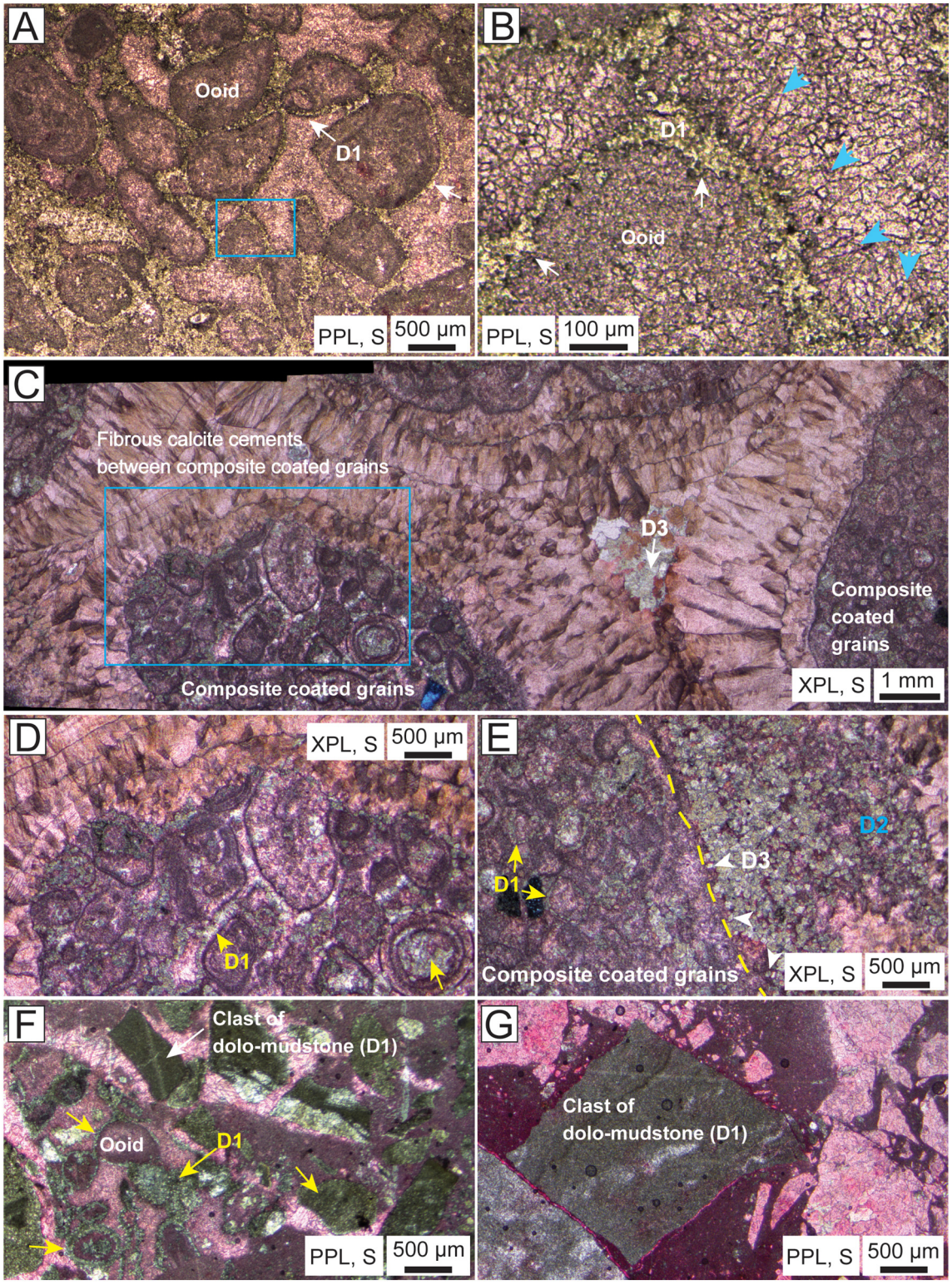

Fig. 10. Photomicrographs of dolomite type 1 (D1) at the platform margin and slope. (A) Ooids are replaced by microcrystalline D1 that surrounds ooids from traverse 1 at the southern margin. The area within the blue box is shown in panel (B) where replacement of D1 results in irregular margins (white arrows) of ooids. The original fibrous isopachous calcite type 1 is still recognizable after recrystallization (blue arrows). (C) Partially dolomitized composite coated grains at the platform margin. Dolomite type 3 (D3) fills the interparticle pores after precipitation of fibrous calcite cements. Details in the rectangle is shown in panel (D) where D1 replaces oolitic cores and isopachous calcite cements around ooids. (E) D1 replaces oolitic cores within composite coated grains versus anhedral to subhedral dolomite type 2 (D2) replaces fibrous calcite cements and euhedral D3 precipitates near the contact between composite coated grains and calcite cements. (F) Dolomitized clasts of oolite and lime mudstone in slope lime breccia from traverse 1. A clast of oolite contains D1 that replaces oolitic cores and isopachous calcite cements around ooids. (G) Dolomitized clasts of lime mudstone in slope lime breccia from traverse 1. S = stained with Alizarin Red S; PPL = plane polarized light; XPL = cross polarized light. (For interpretation of the references to colour in this figure legend, the reader is referred to the web version of this article.)

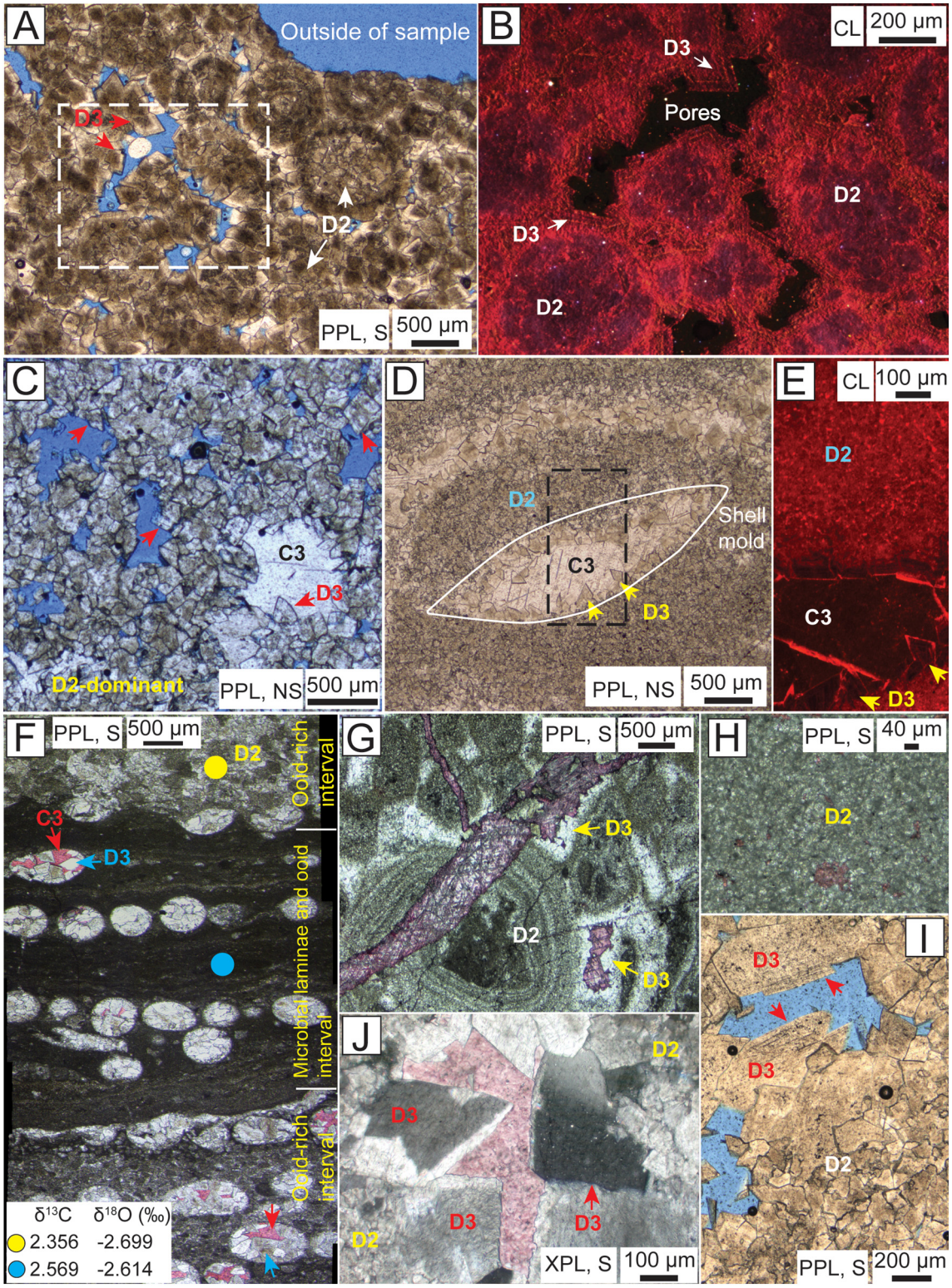

Fig. 11. Photomicrographs of dolomite types 2 (D2) and 3 (D3). (A) Oolite is replaced by cloudy D2 at the platform margin. Relics of ooids are recognizable. Limpid subhedral to euhedral D3 is adjacent to interparticle pores. CL image of the area within the rectangle is shown in panel (B). (C) Fabric-destructive dolostone (oolite) contains intercrystalline and vuggy pores. D3 with curvy outline is pointed by red arrows. The sample was collected at the outcrop shown in Fig. 6B at the platform margin. (D) Dolomitized mollusk packstone at the platform margin. The morphology of shells is preserved. D3 is developed within a shell after meteoric dissolution and the pore inside is eventually filled by calcite type 3 (C3). CL image of the area in the dashed rectangle is shown in panel (E). (F) Dolomitized ooids and microbial laminae in the platform interior. D3 and C3 fill the molds of ooids. $\delta^{18}O$ values of D3 (yellow circle) and dolomitized microbial laminae (blue circle) are not significantly different. (G) D3 fills interparticle and fracture-related pores. (H) Microcrystalline D2 in dolomitized lime mudstone adjacent to fractures. (I) D3 displays curving outline adjacent to pores and anhedral to subhedral D2 is away from pores. (J) D3 showing undulatory extinction and curving outline. PPL = plane polarized light; XPL = cross polarized light; CL = cathodoluminescence light; S = stained with Alizarin Red S; NS = non-stained. (For interpretation of the references to colour in this figure legend, the reader is referred to the web version of this article.)

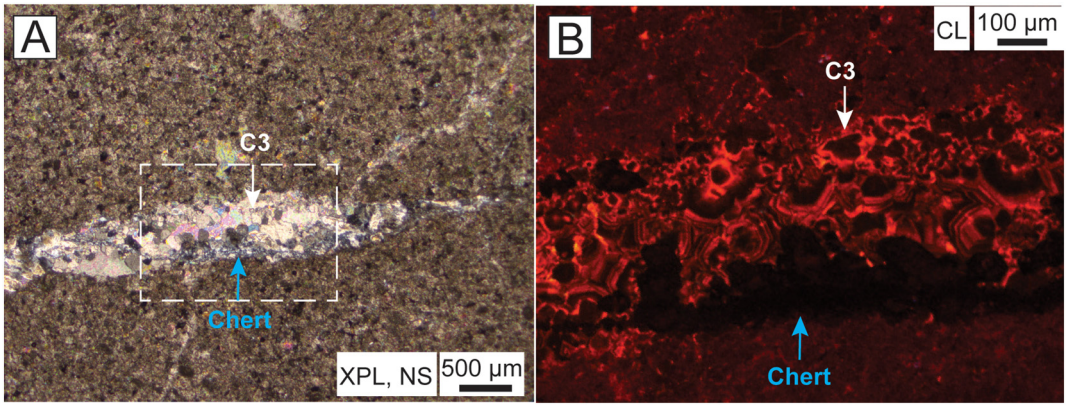

Fig. 12. Photomicrographs of minor diagenetic features. (A) Fractures are subsequently filled by chert cements and calcite type 3 (C3) at the slope. CL image of the area in the rectangle is shown in panel (B). XPL = cross polarized light; CL = cathodoluminescence light; NS = non-stained.

fluid inclusions. Two-phase aqueous fluid inclusions within D2, D3, and C3 were large enough to measure for homogenization temperatures (T_h) and freezing-point depressions (T_m) (Fig. 13A to G).

The T_h values of fluid inclusions in D3 range from 113.4 °C to 237.1 °C, but only five of them are >190 °C (Fig. 13H). Salinities converted from ice final melting temperature (T_m) values by following Bodnar (1993) range from 0.17 to 15.86 wt% NaCl equivalent (Fig. 13I). The T_h values of fluid inclusions in D2 range from 81.2 °C to 175 °C (Fig. 13H). Salinities exhibit a wide range from 2.4 to 16.61 wt% NaCl equivalent (Fig. 13I). Fluid inclusions with salinities <3.5 wt% NaCl equivalent in dolomite (Fig. 13I) all came from one sample, RBT-207, from the Rungbao section near the platform margin.

The T_h values of secondary FIAs in later-stage blocky C3 from the sample, RBT-215, range from 55 °C to 109.2 °C (Fig. 13H). Two secondary FIAs record T_h values from 55 °C to 65 °C and from 97 °C to 109.2 °C, respectively. Due to vapor bubble metastability, salinity values from the two secondary FIAs in C3 could be estimated using the ice nucleation temperatures (−38 °C to −43 °C) by following the method of Wilkinson (2017). They are estimated to have a salinity of ≤2.6 wt% NaCl equivalent (Fig. 13I). A few calcite crystals contained limited 3-D networks of apparent all-liquid aqueous inclusions, suggesting entrapment below about 50 °C (Fig. 13H; Goldstein and Reynolds, 1994).

In one thin section containing both D2 and D3 dolomite crystals, a distinctive trend in T_h values was identified, increasing from replacive dolomite core (D2) to dolomite cement edge (D3) (Fig. 14A). The T_h of D2 ranges from ~100 °C to 125 °C, whereas the T_h of D3, spans from ~130 °C to 190 °C. In addition, the T_h of fluid inclusions in D3 increases from inner to outer rims (Fig. 14A), whereas increased T_m of fluid inclusions suggests that the salinities decrease (Fig. 14B).

4.4. Trace element concentrations

The Fe, Mn, and Sr concentrations measured from host limestone and the three types of dolomite are shown in Fig. 15. The Fe concentrations of host limestone range from 106 to 1975 ppm with a mean value of 485 ppm. The Fe concentrations of D1 are from 175 to 507 ppm with a mean value of 316 ppm. The Fe concentrations in D2 are from 18 to 5605 ppm with a mean value of 801 ppm. The Fe concentrations of D3 range from 18 to 577 ppm with a mean value of 171 ppm. The Mn concentrations of host limestone range from 0.5 to 114 ppm with a mean value of 45 ppm. The Mn concentrations of D1 are from 27 to 105 ppm with a mean value of 75 ppm. The Mn concentrations in D2 are from 5 to 307 ppm with a mean value of 100 ppm. The Mn concentrations of D3 range from 10 to 240 ppm with a mean value of 83 ppm. The Sr concentrations of host limestone range from 77 to 597 ppm with a mean value of 195 ppm. The Sr concentrations of D1 are from 200 to 463 ppm with a mean value of 303 ppm. The Sr concentrations in D2 are from 20 to 695 ppm with a mean value of 212 ppm. The Sr concentrations of D3 range from 7 to 745 ppm with a mean value of 220 ppm.

The Fe, Sr, and Mn concentrations measured from host limestone and the three types of dolomite do not cluster into distinct fields in the bivariate plots and the fields overlap (Fig. 15). Compared to the other two categories of dolomite, D2 has the widest range of Fe, Sr, and Mn values (Fig. 15). Analysis of variance (ANOVA) suggests Sr and Mn concentrations, in contrast to Fe concentrations (p-value = 0.03 for Fe), do not differ significantly among different types of dolomite and limestone (p-value = 0.07 for Mn; p-value = 0.72 for Sr).

4.5. Carbon and oxygen isotopes

The $\delta^{13}C$ and $\delta^{18}O$ values measured from host limestone and the three types of dolomite are shown in Fig. 16A. The $\delta^{13}C$ values of host limestone range from 0.17 ‰ to 2.98 ‰ with a mean value of 1.36 ‰. The $\delta^{13}C$ values of D1 is from 1.73 to 1.97 ‰ with a mean value of 1.85 ‰. The $\delta^{13}C$ values of D2 are from −1.02 to 4.91 ‰ with a mean value of 2.05 ‰. The $\delta^{13}C$ values of D3 ranges from 1.92 to 2.84 ‰ with mean values of 2.39 ‰. The $\delta^{18}O$ values of host limestone range from −10.97 to −0.71 ‰ with a mean value of −4.95 ‰. The $\delta^{18}O$ values of D1 are from −3.70 to −3.07 ‰ with a mean value of −3.43 ‰. The $\delta^{18}O$ values of D2 are from −11.73 to −0.87 ‰ with a mean value of −4.30 ‰. The $\delta^{18}O$ values of D3 range from −10.22 to −1.75 ‰ with mean values of −3.98 ‰.

The distributions of $\delta^{13}C$ and $\delta^{18}O$ values of D1, D2, D3, and host limestone generally overlap. The range of $\delta^{13}C_{\_VPDB}$ (−4 ‰ to 8 ‰) was documented by Payne et al. (2004) for the GBG and confirmed in later studies (Meyer et al., 2011; Tong et al., 2007). In contrast to $\delta^{13}C$ (p-value = 0.01), $\delta^{18}O$ does not show evidence of significant differences among different types of dolomite and limestone (p-value = 0.21) based on ANOVA. (Fig. 16). The magnitude of the values is consistent with previous findings on the GBG (Kelley et al., 2020; Meyer et al., 2011).

4.6. Strontium isotopes

$^{87}Sr/^{86}Sr$ values measured for limestone and three types of dolomite from the Lower Triassic strata of the GBG range from 0.70757 to 0.70919. The $^{87}Sr/^{86}Sr$ values of limestone are generally similar to dolostone (Fig. 17). Limestone has Sr isotopic ratio values ranging from 0.70801 to 0.70852. $^{87}Sr/^{86}Sr$ values of D1 spans from 0.70795 to

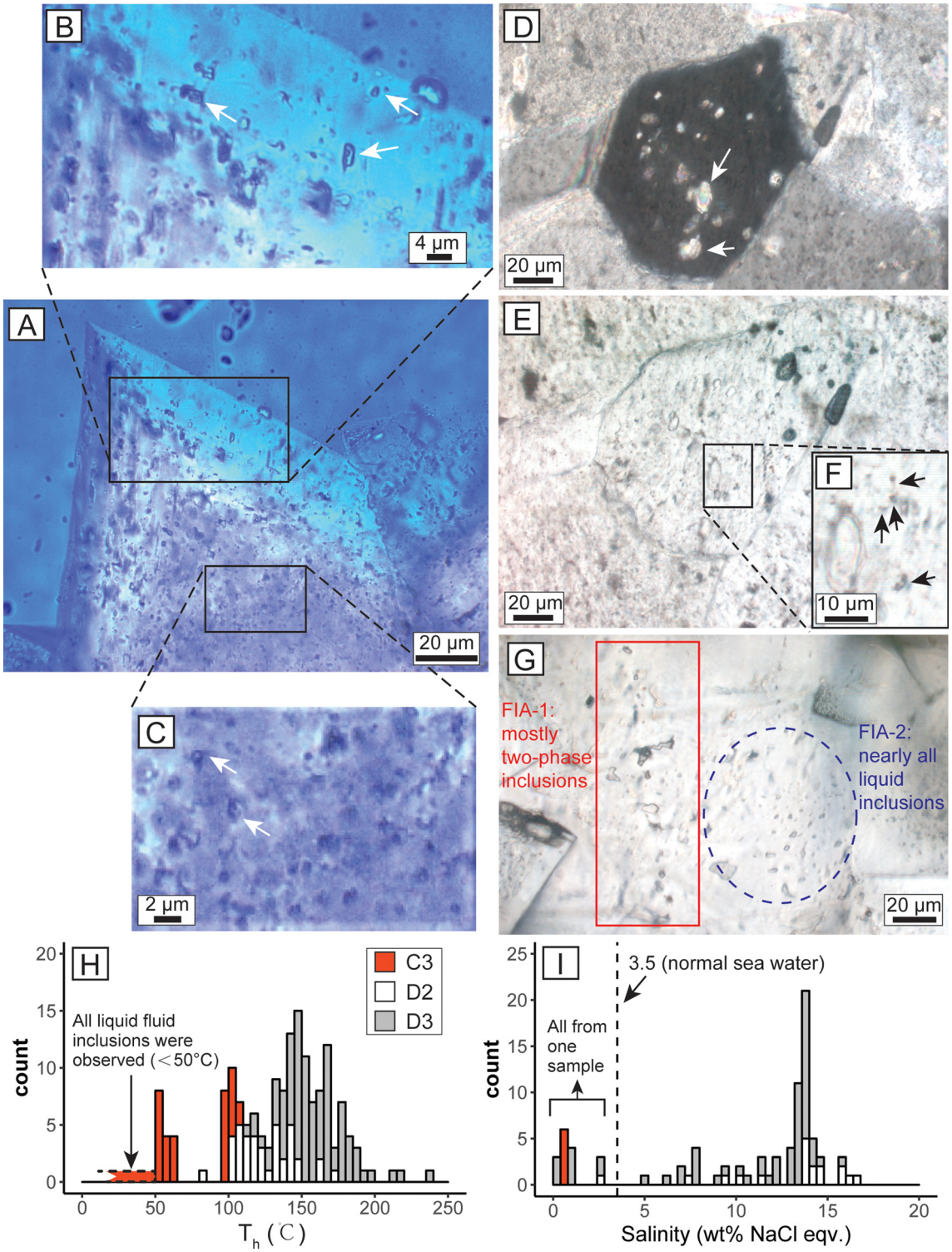

Fig. 13. Microthermometry and petrography of fluid inclusions in dolomite types 2 (D2) and 3 (D3), and calcite type 3 (C3) in the dolomitized Lower Triassic succession of the GBG. (A) to (C) Two-phase aqueous fluid inclusions (white arrows) from the rim and core of a D3. (D) to (F) Two-phase aqueous fluid inclusions (black arrows) inside of an anhedral D2 that contains birefringent relics of precursor calcite (white arrows) supporting a replacive origin (panel D; cross polarized light). (G) Fluid inclusions in C3. (H) Stacked histogram of homogenization temperatures (T_h) of aqueous fluid inclusions. All liquid primary fluid inclusion associations were observed in C3 from a sample, RBT-215, suggesting some C3 were formed <50 °C. (I) Stacked histogram of salinity of aqueous fluid inclusions.

0.70801. Sr isotopic ratios of D2 are from 0.70757 to 0.70919 and D3 are from 0.70790 to 0.70812. Most of the $^{87}Sr/^{86}Sr$ values are consistent with the reported values of Early Triassic seawater (McArthur et al., 2001; Song et al., 2015). Two D2 samples are slightly higher than the reported range of $^{87}Sr/^{86}Sr$ values of the Early Triassic seawater (Fig. 17). Furthermore, mostly $^{87}Sr/^{86}Sr$ values of the dolomite and limestone samples in this study are significantly lower than that of the Precambrian basement (the Yunkai and Jiangnan massifs; Fig. 1) and deep basinal brine in the Nanpanjiang Basin (Wang et al., 2016; Yang et al., 2019; Zhang and Wang, 2019; Fig. 17).

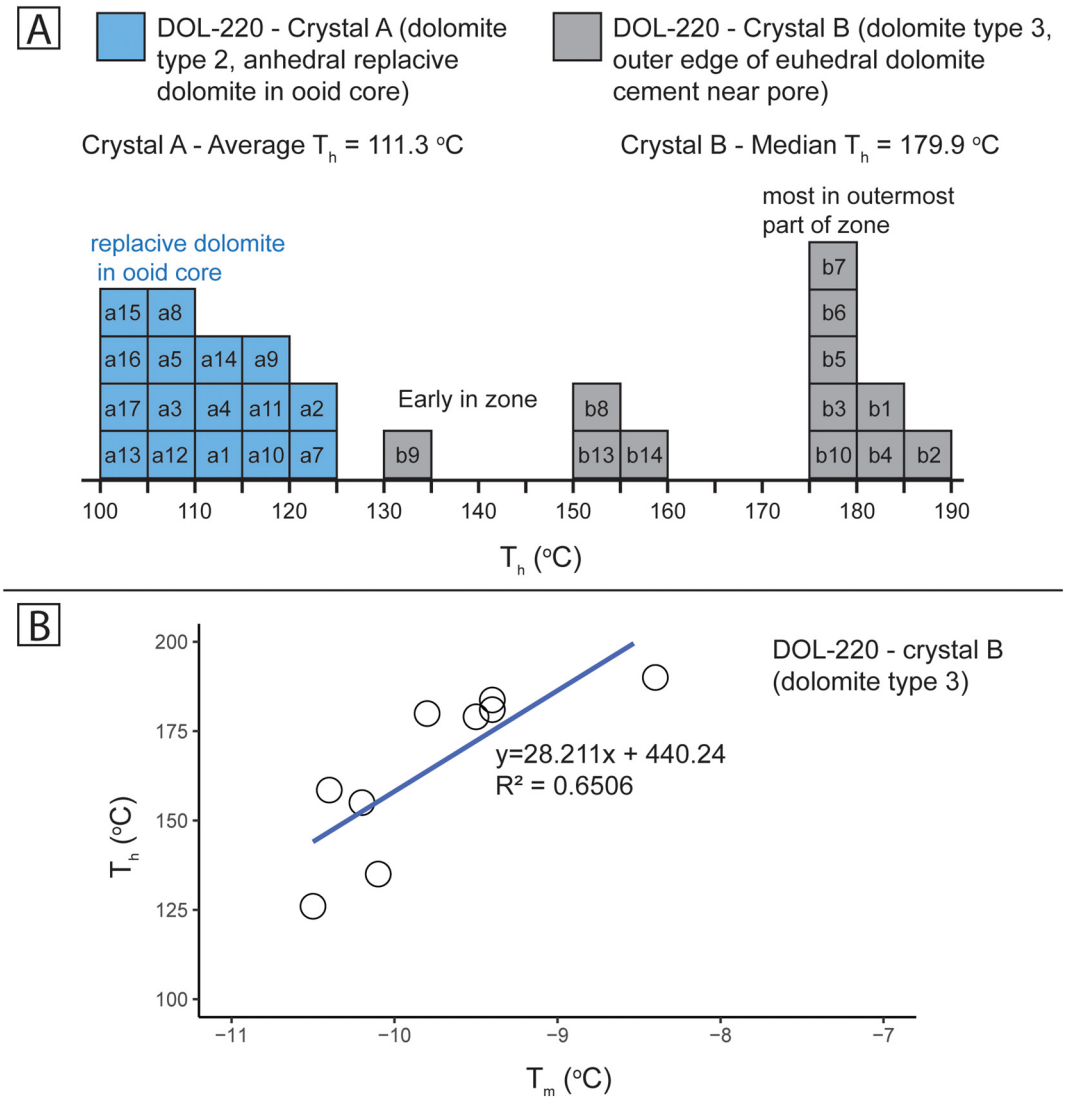

Fig. 14. Microthermometry of fluid inclusions in a dolostone sample (DOL-220). (A) Homogenization temperature of FIAs in one dolomite type 2 and one dolomite type 3. (B) T_h versus T_m of FIAs in one dolomite type 3.

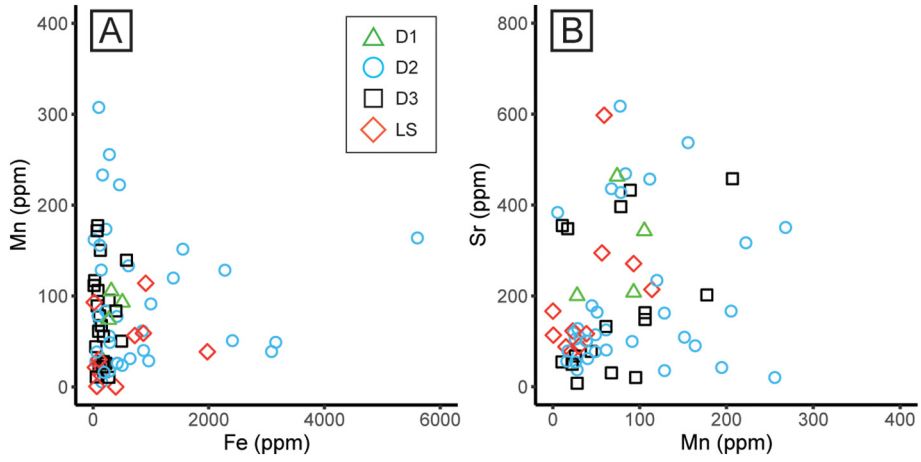

Fig. 15. Relative concentrations of trace elements (iron, manganese, and strontium) in the Lower Triassic limestone (LS), dolomite types 1 (D1), 2 (D2), and 3 (D3) from the dolomitized Lower Triassic succession of the GBG. Element concentrations in a few measured samples are below detection limit (see supplementary data).

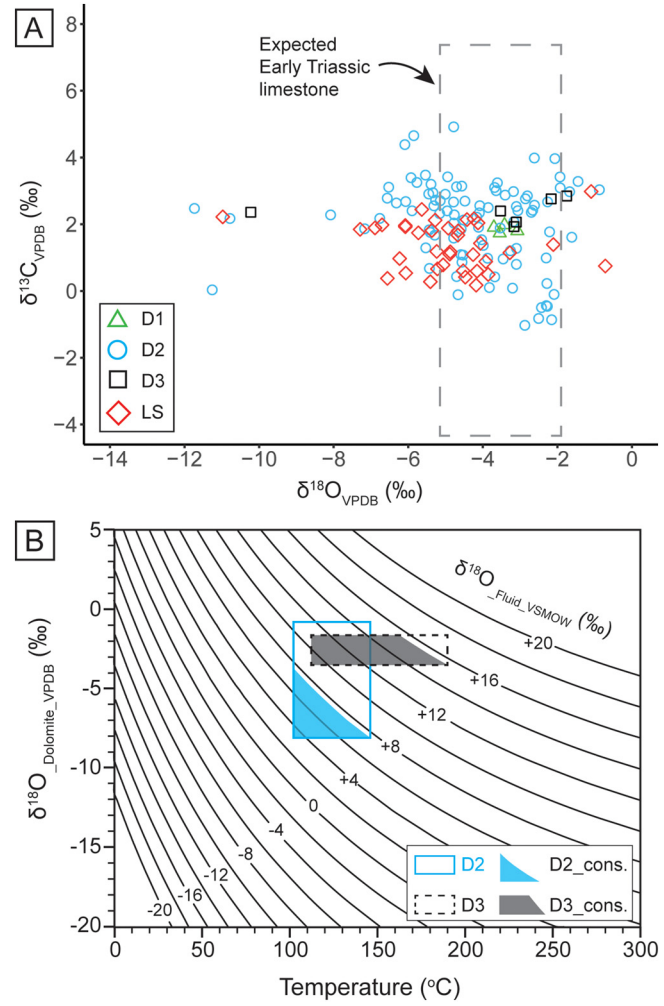

Fig. 16. Carbon and oxygen isotopic composition of carbonates from the dolomitized Lower Triassic succession of the GBG. (A) Carbon and oxygen isotopic composition of the Lower Triassic limestone (LS), dolomite types 1 (D1), 2 (D2), and 3 (D3). The range of $\delta^{18}O_{\_VPDB}$ of Early Triassic limestone (−1.9 to −5.5 ‰) in isotopic equilibrium with coeval seawater is calculated from coeval tropical shallow water temperature (20 to 38 °C; Sun et al., 2012) and assuming the Early Triassic was ice-free ($\delta^{18}O_{\_VSMOW} = -1$ ‰). (B) Graph displaying the ranges of $\delta^{18}O_{\_VSMOW}$ of dolomitizing fluid in equilibrium with D2 and D3 using $10^3 \ln\alpha_{dolomite\text{-}fluid} = 3.14 \times 10^6 T^{-2} - 3.14$ (Horita, 2014) based on $\delta^{18}O_{\_VPDB}$ of D2 and D3 as well as T_h ranges of D2 (102 to 147.2 °C) and D3 (113.4 to 190 °C). $\delta^{18}O_{\_VSMOW}$ values from 2.8 to 7.5 ‰ (blue shade) and from 8.8 to 15.4 ‰ (gray shade) are interpreted to reflect a conservative range of dolomitizing fluid in equilibrium with D2 and D3.

5. Discussion

5.1. Paragenetic sequence

Field relationships, petrography, and microthermometry suggest that the Lower Triassic limestone of the GBG was altered during three stages (Fig. 18).

5.1.1. Stage 1

Early marine micritic envelopes and isopachous C1 are important diagenetic fabrics because of their wide distribution across depositional environments and precipitation shortly after sediment deposition at a temperature likely similar to that of coeval surface seawater. Early Triassic surface seawater temperatures in the Nanpanjiang Basin ranged from 32 to 38 °C (Sun et al., 2012). Gypsum pseudomorphs formed through evaporation are particularly abundant in mud-rich tidal flat environments on the platform top (Fig. 9A and C). Isopachous C1 fills interparticle pores of oolitic grainstone (Figs. 8A and 10C), suggesting that it developed soon after deposition of ooids. C2 precipitated after mechanical compaction as indicated by the fact that it engulfs concave-convex grain contacts (Fig. 8B). C2 infills primary interparticle, fenestral, and shelter pores. In addition to mechanical compaction, grains and mud also went through neomorphism. Lower Triassic ooids usually have alternating cortical layers of dark micritic calcite with bright, coarser calcite (Fig. 8A). Cortices of the bright, coarse-crystalline calcite have been inferred to result from neomorphism and to have originally been composed of aragonite (Lehrmann et al., 2012). Oolitic molds formed in the platform interior result from meteoric dissolution (Fig. 11F; Lehrmann et al., 1998) and are often filled by later diagenetic phases.

D1, containing apparent single-phase fluid inclusions (formed at <50 °C from Goldstein and Reynolds, 1994) and being preserved with gypsum (Fig. 9A and C; Table 1), cross-cuts bedding planes (Fig. 6E and F), suggesting that it formed after deposition of sediments. Moreover, slope breccia at the southern margin contains lime micrite and dolomitized clasts of oolite, mudstone, and microbialite (D1; Table 1; Fig. 7D to F). In the matrix-supported breccia, only clasts are dolomitized (Figs. 7E and 10G) and the micrite is undolomitized, which indicates that the dolomitization occurred in near-surface or shallow burial environment (see origin of D1 below) before the resultant dolomitized facies were eroded and transported as clasts to the slope due to margin failure in the Middle Triassic (Lehrmann et al., 2020).

The combination of early marine C1 (Sun et al., 2012), concave-convex grain contacts engulfed by C2, D1 containing single-phase fluid inclusions, timing of dolomitization (D1) earlier than Middle Triassic margin collapse (i.e., the platform did not get buried by siliciclastic turbidite until Late Triassic in Fig. 3B) suggests the diagenetic events in stage 1 occurred during an eogenetic phase (near-surface to shallow burial).

5.1.2. Stage 2

Stylolites and fractures postdate D1 because they cross-cut D1 and other diagenetic phases that were formed during eogenesis (Figs. 8B and 9F). D2 and D3 are developed in various fabrics and depositional environments. D2 mostly replaced host limestone prior to fractures, but some D2 replacing limestone adjacent to fractures and D3 precipitating on the walls of fractures (Table 1; Figs. 7H and 11G) demonstrate their formation postdates fractures. In addition, the high T_h of fluid inclusions in D2 and D3 (~100 to 190 °C) suggests that they formed in a deep-burial environment (Fig. 13H). Chert cement is rare, but it did infill fractures (Fig. 12A).

D3 in fractures within slope facies experienced localized dedolomitization as indicated by partially leached and calcitized dolomite rhombohedrons (Table 1; Fig. 8C). Although dedolomitization is often interpreted to have occurred in an eogenetic or telogenetic diagenetic environment where excess calcium is supplied from dissolution of evaporite minerals by meteoric water (Schoenherr et al., 2018), the rarity of dedolomitization within the fractures at the GBG more likely implies that it was formed during mesogenesis, because influx of meteoric water during eogenesis or telogenesis tends to non-selectively replace more dolomitized fabrics rather than limited areas of D3 in fractures. The formation time of D2 and D3 relative to fractures and high T_h in their fluid inclusions suggest that these diagenetic events in stage 2 happened in a mesogenetic (intermediate to deep burial) environment.

5.1.3. Stage 3

Clear, blocky C3 usually infills the remaining pores in fractures or engulfs euhedral D3 (Fig. 8D and G), suggesting that C3 was formed after D3 and D2 (Table 1). T_h of secondary fluid inclusions (<50 °C, 55–65 °C, 97–109 °C in Fig. 13H), brackish water salinity (Fig. 13I), and later

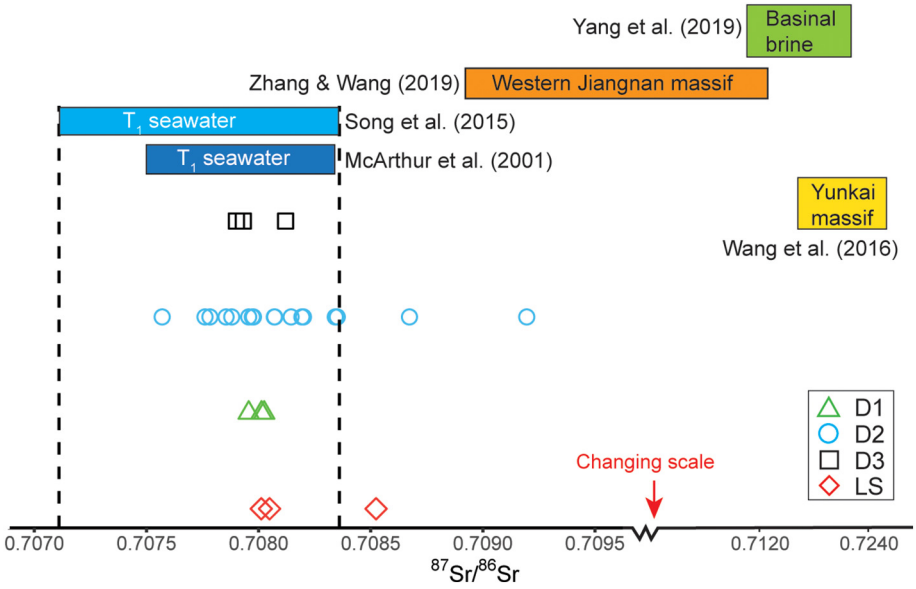

Fig. 17. Strontium isotopic ratio ($^{87}Sr/^{86}Sr$) of the Lower Triassic limestone (LS), dolomite types 1 (D1), 2 (D2), and 3 (D3) from the dolomitized Lower Triassic succession of the GBG. $^{87}Sr/^{86}Sr$ ranges of the Early Triassic seawater (McArthur et al., 2001; Song et al., 2015), the Jiangnan massif and Yunkai massif (Wang et al., 2016; Zhang and Wang, 2019), and deep basinal brine in the Nanpanjiang basin is from (Yang et al., 2019) are used for comparison and constraint on the origin of dolomite.

paragenetic sequence of C3 relative to D3 and D2 together suggest that C3 formed in a deep burial or a late, near-surface (telogenetic) environment.

5.2. Significance of strontium isotope ratios

Because strontium does not fractionate under pressure, temperature, evaporation and microbial processes (Faure and Powell, 1972), and $^{87}Sr/^{86}Sr$ of seawater has a well-characterized secular trend through geologic time (Veizer et al., 1999), the $^{87}Sr/^{86}Sr$ recorded in marine carbonate rocks have been used as a tool to date strata, correlate stratigraphic sections, and constrain the nature of magnesium-rich fluid that drove dolomitization (Edwards et al., 2015; Hendry et al., 2015). The $^{87}Sr/^{86}Sr$ of seawater was approximately 0.7071 at the time of the Permian/Triassic transition and eventually increased to approximately 0.7084 by the end of the Early Triassic (Korte et al., 2003; Martin and Macdougall, 1995; Song et al., 2015). $^{87}Sr/^{86}Sr$ values of samples measured for this study are all higher than the known range for Late Permian seawater and mostly overlap the reported range of the Early Triassic seawater, with the exceptions of one limestone and two D2 samples (Table 1; Fig. 17). The limestone sample (RL-469.2) and two D2 samples were collected near fractures (e.g., Fig. 7H). Their $^{87}Sr/^{86}Sr$ ratios are slightly higher than other samples and are interpreted to likely result from radiogenic strontium released from potassium-bearing minerals in the deep-basin environment during compaction (see below for detail). In addition, mostly $^{87}Sr/^{86}Sr$ ratios of the dolomite and limestone samples in this study are significantly lower than that of the Precambrian basement (the Yunkai and Jiangnan massifs; Fig. 1) and deep basinal brine in the Nanpanjiang Basin (Wang et al., 2016; Yang et al., 2019; Zhang and Wang, 2019; Fig. 17). Overall, the majority of $^{87}Sr/^{86}Sr$ values suggest that D1, D2, and D3 retain the signal of an Early Triassic seawater source (see more interpretation below).

5.3. Origin of dolomite

5.3.1. Origin of D1

D1 mainly occurs in the platform interior and platform margin. It is also preserved as dolomitized clasts within slope lime breccia (e.g., Table 1; Figs. 7D and E, 10F and G). The cumulative thickness of the massive dolostone decreases from the platform interior to the basin (Fig. 4). The formation of massive dolostone requires a long-lasting and efficient flow system to supply sufficient magnesium and carbonate ions (Machel, 2004). Therefore, positions of dolostone in conjunction with spatial thickness variations have been used to infer the general flow pathway of dolomitizing fluid (Kaufman, 1994; Warren, 2000). Along the flow path of the dolomitizing fluid, the concentration of magnesium ions generally decreases because dolomitization removes magnesium ions from the fluids. Accordingly, massive dolostone is expected to be generally thicker near the source of magnesium ions and thinner in more distal settings (Garcia-Fresca et al., 2012; Wang et al., 2015). The spatial thickness variation of dolostone from the interior (~650 m at Dajiang section) to the margin (~250 m at Rongling section; Table 1; Fig. 4) suggests that the circulation pattern of dolomitizing fluid originated from the platform top and migrated downwards the interior and towards the margin.

Slope clast-supported and matrix-supported breccia near the southern margin of the GBG is not pervasively dolomitized (traverse 1 in Fig. 3A). The breccia formed because of platform margin collapse in the Middle Triassic (Lehrmann et al., 2020). The breccia contains dolomitized clasts from the platform interior and margin, including lime mudstone, fenestral limestone, microbialite, and oolite (Fig. 7D to G; Li et al., 2021); however, the matrix of the breccia is undolomitized. The breccia suggests that the dolomitization occurred in a near-surface or shallow-burial environment in the Early Triassic before the resultant dolomitized facies were eroded and transported as clasts to the slope due to margin failure in the Middle Triassic.

Fluid inclusions in D1 within clasts of dolo-oolite in slope lime breccia are small and single-phase (Table 1). The single-phase liquid inclusions suggest their formation temperature is significantly <50 °C (Goldstein and Reynolds, 1994), compatible with the near-surface and shallow burial environment when reflux occurred. Furthermore, faults were not developed in the studied area and the GBG was not buried by basinal siliciclastic turbidites until the Late Triassic, which suggests that D1 did not result from deep burial or hydrothermal dolomitization.

Oxygen isotope ratios from diagenetically resistant conodont apatite suggest that the temperature of shallow seawater within the Nanpanjiang Basin ranged from 32 to 38 °C during the Early Triassic (Sun et al., 2012). The precipitation of gypsum in the dolomitized mud-rich facies of the platform interior (Table 1; Fig. 9A and C) demonstrates episodes of enhanced evaporation on the platform

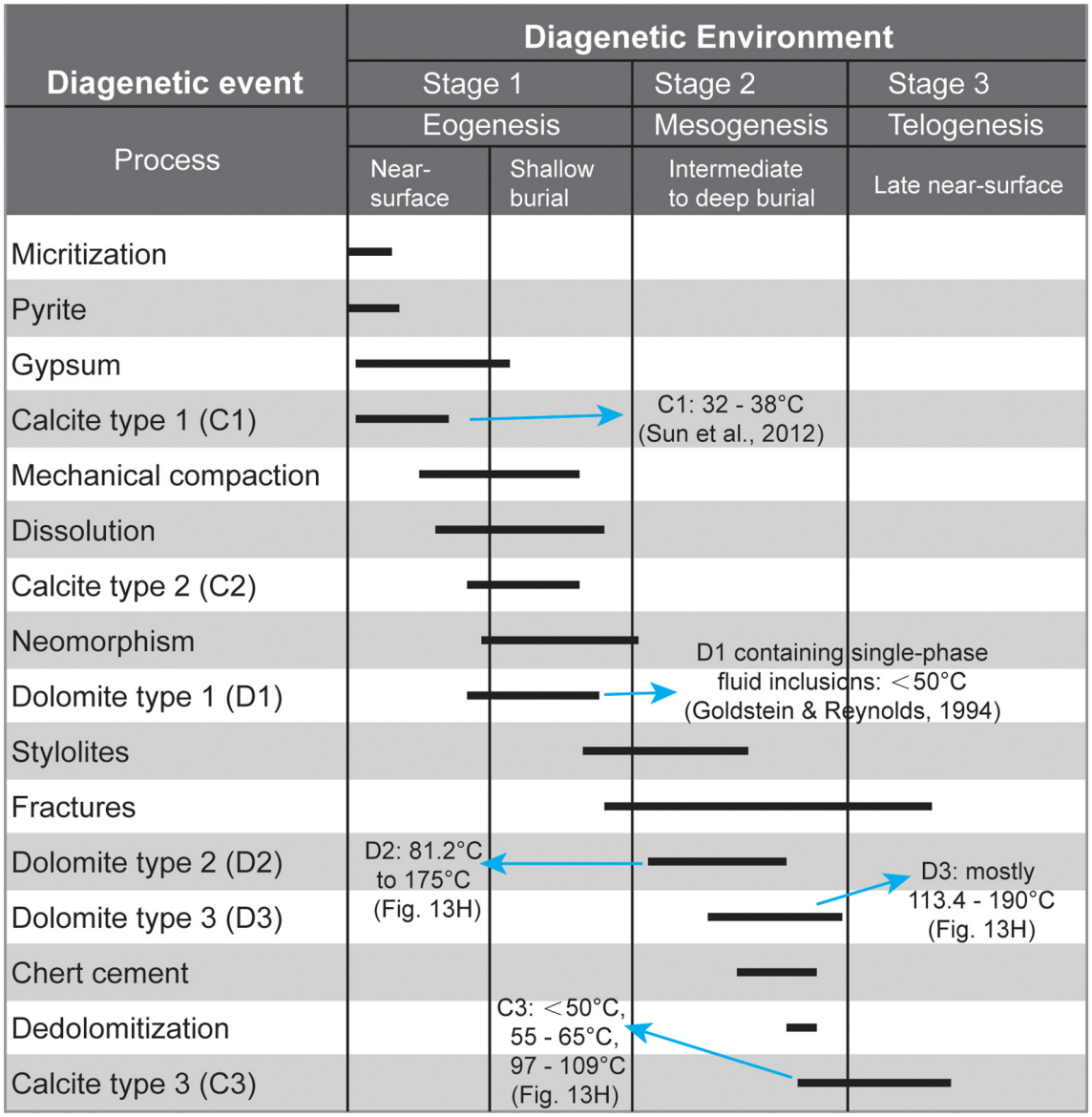

Fig. 18. Paragenetic sequence of the Lower Triassic succession of the GBG.

top. Karst terrane hampers efforts to trace features laterally on the GBG to determine the continuity of the evaporite, but many laterally continuous, brecciated intervals are developed in the coeval facies (Anshun Fm.) of the adjacent Yangtze Platform (Enos et al., 2006). The brecciated intervals, containing pseudomorphs of gypsum crystals, suggest they formed through solution and collapse of evaporite (Enos et al., 2006). Furthermore, the low diversity fauna of bivalves, gastropods, and spirorbid worms from the platform interior suggests that seawater circulation on the platform top was restricted in the Early Triassic, potentially due to the build-up of oolitic shoals at the platform margin (Lehrmann et al., 1998). Restricted circulation on the platform top and high seawater temperatures could facilitate evaporation of platform-top seawater. However, the $\delta^{18}O$ values of D1 appear to be more comparable to those of host limestone and seawater (Fig. 16A) than expected ^{18}O-enriched values of dolomite resulting from evaporation process, because the expected $\delta^{18}O$ values of dolomite relating to evaporation process would have been at least 2 to 4 ‰ heavier than coeval limestone if the equilibrium fractionation ($\delta^{18}O_{\_dolomite}$ - $\delta^{18}O_{\_calcite}$) is 3 ‰ at the same temperature (Budd, 1997; Land, 1980). The relatively low $\delta^{18}O$ values of D1 likely suggest that pristine values had been reset to be ^{16}O-enriched due to geothermal heating after the GBG was buried by marine turbidites (Fig. 3).

In addition to the development of gypsum, D1 has $^{87}Sr/^{86}Sr$ ratios consistent with that of coeval seawater (Fig. 17), further indicating that the dolomitizing fluids formed via the evaporation of seawater on the platform top during the Early Triassic.

Therefore, the combination of spatial thickness variation of dolostone, slope breccia with dolomitized clasts and undolomitized micrite, single-phase fluid inclusions in D1, co-occurrence with evaporates, and $^{87}Sr/^{86}Sr$ values of D1 suggests D1 formed by seepage-reflux of the Early Triassic evaporated seawater.

5.3.2. Origin of D2

D2 developed in various fabrics and depositional environments, such as peloidal packstone in the interior, oolite and mollusk packstone at the platform margin (Fig. 11A and D), and slope breccia (Fig. 7G). It also occurs adjacent to fractures (Table 1; Fig. 7G and H). T_h of two-phase FIAs in D2 suggests that they were usually formed at temperatures >100 °C (Fig. 13H). High T_h measured from some consistent FIAs in D2 that contain calcite precursor (Fig. 13D) and display clotted

texture (Fig. 11B) suggests that D2 formed by replacement related to a burial fluid reaching 100 to 125 °C (Fig. 14A). Microscopic dolomite adjacent to each fluid inclusion within a D2 crystal was too small to sample for isotopic analysis in this study. Accordingly, correlating $\delta^{18}O$ variations of dolomite adjacent to each measured fluid inclusion in a D2 crystal is unavailable; and measured $\delta^{18}O$ values of dolomite reveal weighted average isotopic compositions of D2 and any other nearby phases. Mn/Sr and $\delta^{18}O$ values are commonly used to assess the degree of diagenetic alteration of marine carbonates. Samples with Mn/Sr < 3 and/or $\delta^{18}O > -10$ ‰ are suggested to be less altered (Kaufman and Knoll, 1995). Samples in the study mostly yielded Mn/Sr < 3 and $\delta^{18}O > -8$ ‰, suggesting most of them are not significantly altered whereas several host limestone, D2, and D3 samples that have Mn/Sr > 3 and/or relatively low $\delta^{18}O$ values (<−10 ‰; Fig. 16A) are unacceptably altered. Except for the unacceptably altered samples, the lower end of $\delta^{18}O_{\_VPDB}$ of D2 (−8.0 ‰) and T_h range of D2 (102 to 147.2 °C) were used to calculate $\delta^{18}O_{\_VSMOW}$ of the dolomitizing fluid (2.8 ‰ to 7.5 ‰ for D2) by applying Horita's (2014) correction. Because the lowest $\delta^{18}O_{\_VPDB}$ values of dolomite do not necessarily correlate with the highest T_h of fluid inclusions, the $\delta^{18}O_{\_VSMOW}$ of 2.8 ‰ to 7.5 ‰ is interpreted to reflect a conservative range of the dolomitizing fluid in equilibrium with D2 (blue shaded region in Fig. 16B).

High T_h of FIAs in D2 and its relation to fractures suggest that it formed in a deep burial environment (Table 1; Figs. 5F and 7H). Because the younger siliciclastic turbidites directly overlying the GBG have been partly eroded away, the complete thickness of the turbiditic succession is estimated from the nearby area (> 3 km thick near Zhenfeng). The maximum burial depth for the base of the GBG was approximately 6 km, reflecting both the accumulation of younger carbonates on the platform (~3 km) and subsequent burial by siliciclastic turbidites (>3 km) (Lehrmann et al., 1998, 2015). This estimate is generally compatible with fluid inclusion thermometry (100 to 190 °C in Fig. 13H for D2 and D3), assuming an average surface seawater temperature at 35 °C during the Early Triassic (Sun et al., 2012) and a geothermal gradient of 25 °C/km. Moreover, the burial history and T_h indicates that D2 did not form prior to the Carnian (Table 1).

The salinities of fluid inclusions in D2 show that most of the dolomitizing fluid was more saline than seawater (~5 to 17 wt%, NaCl equivalent), although some inclusions in one dolostone sample near the platform margin indicate a brackish source (Fig. 13I). Because ooids were leached by meteoric freshwater in the platform interior (Fig. 11F; Lehrmann et al., 1998), oolitic shoals at the platform margin with higher topography also likely experienced meteoric dissolution. Meteoric water may have been locally preserved in pores at the margin and mixed with the dolomitizing brine from the basin, diluting its salinity, which explains the low salinity of localized fluid inclusions at the platform margin. Alternatively, this sample might contain unrecognized secondary (or leaked and refilled) fluid inclusions entrapped long after dolomitization, which could have salinities similar to secondary FIAs observed in C3.

$^{87}Sr/^{86}Sr$ values of D2 are within the range of Early Triassic seawater except for two data points (Fig. 17), suggesting that the dolomitizing fluids with high T_h originating from a deep burial environment generally retain the strontium isotopic properties of Early Triassic seawater (Table 1). The two outliers are interpreted to result from incorporation of radiogenic Sr of the Late Triassic basinal siliciclastic sediments coming from the Jiangnan Massif (Fig. 17) when the dolomitizing fluids escaped from the Lower Triassic basinal carbonate strata (see more details about a proposed model below). Absence of faulting in the studied area also argues against the scenario in which D2 has a hydrothermal origin from deep, over-pressured fluids migrating via faults.

Consequently, the combination of high T_h, occurrence nearby fractures, $^{87}Sr/^{86}Sr$ values of D2, and absence of faulting in the studied area suggest that formation of D2 was driven by burial dolomitization related to fluids of the modified Early Triassic seawater origin trapped in the Lower Triassic basinal carbonate strata (Table 1).

5.3.3. Origin of D3

D3, often displaying undulatory extinction (e.g., saddle dolomite in Fig. 11J), co-occurs with D2 in various fabrics and depositional environments, such as the dolomitized oolitic grainstone above the thin-bedded lime mudstone in the platform interior (Dajiang section in Fig. 4 and Fig. 5C), dolomitized oolite and mollusk packstone at the platform margin (Fig. 11A and D), and dolomitized lime mudstone or breccia at the slope (e.g., Fig. 12A). D3 is often developed in fractures (Table 1; Fig. 7H), meaning it formed later than the fractures. T_h values of two-phase FIAs in D3, ranging from 113.4 to 190 °C, suggest that D3 was also formed in a deep burial environment (Table 1).

T_h of fluid inclusions sometimes varies substantially within a single D3 crystal (e.g., ~130 to 190 °C in Fig. 14B), and microscopic dolomite adjacent to each fluid inclusion within a D3 crystal was too small to sample for isotopic analysis in this study. Therefore, correlating $\delta^{18}O$ variations of dolomite adjacent to each measured fluid inclusion in a D3 crystal is also unavailable; and measured $\delta^{18}O$ values of dolomite reveal weighted average isotopic compositions of D3. Except for one unacceptably altered D3 samples ($\delta^{18}O_{\_VPDB} < -10$ ‰), lower end of $\delta^{18}O_{\_VPDB}$ of D3 (−3.5 ‰) as well as T_h range of D3 (113.4 to 190 °C) were used to calculate $\delta^{18}O_{\_VSMOW}$ of the dolomitizing fluid (8.8 ‰ to 15.4 ‰ for D3) by applying Horita's (2014) correction. Because the lowest $\delta^{18}O_{\_VPDB}$ values of dolomite do not necessarily correlate with the highest T_h of fluid inclusions, the $\delta^{18}O_{\_VSMOW}$ of 8.8 ‰ to 15.4 ‰, is interpreted to reflect a conservative range of the dolomitizing fluid in equilibrium with D3 (gray shaded region in Fig. 16B). The $\delta^{18}O$ values of D2 along fractures are lighter than those of adjacent limestone (e.g., Fig. 7H).

The salinities of fluid inclusions in D3 show that most of the dolomitizing fluid was more saline than seawater (~5 to 17 wt%, NaCl equivalent), although some inclusions in one dolostone sample near the platform margin might indicate a brackish source (Fig. 13I). $^{87}Sr/^{86}Sr$ values of all D3 are also within the range of Early Triassic seawater (Fig. 17). The combination of salinities, $^{87}Sr/^{86}Sr$ ratios, petrographic features, co-occurrence with D2, and microthermometry suggest that the dolomitizing fluids in equilibrium with D2 and D3 are the same: they originated from Early Triassic seawater-like fluids that were trapped in the Lower Triassic basinal carbonate sediments (Table 1).

5.4. Overlapping geochemical fields

Geochemical fields, including trace element concentrations and oxygen isotope ratios, of the three types of dolomite overlap and ANOVA shows there is no evidence of significant differences in $\delta^{18}O$, Sr, and Mn among the three types of dolomite and limestone. The Lower Triassic dolostone is interpreted to have resulted from reflux dolomitization with subsequent burial dolomitization (see origin of dolomite above). The extent of diagenetic alteration of marine carbonates is often evaluated by Mn/Sr and $\delta^{18}O$ values. Mn/Sr < 3 and/or $\delta^{18}O > -10$ ‰ are used to be indicators of less altered samples (Kaufman and Knoll, 1995). Samples in the study mostly yielded Mn/Sr < 3 and $\delta^{18}O > -8$ ‰, suggesting they did not undergo significant diagenetic alteration except for several unacceptably altered host limestone, D2, and D3 samples that have Mn/Sr > 3 and relatively low $\delta^{18}O$ values (<−10 ‰; Supplementary Data).

Because the slightly altered Early Triassic seawater-like fluid was initially trapped in Lower Triassic basinal carbonate sediments and then expelled into the adjacent platform owing to progressive burial, the $\delta^{18}O$ of the seawater-like fluid would be influenced by water-rock interactions and increasing temperature during the burial and migration, causing relative enrichment of ^{18}O in the dolomitizing fluid and depletion of ^{18}O in the carbonate minerals (Land, 1980). Consequently, the water-rock interactions and high temperature reasonably explain why the altered Early Triassic seawater-like fluid during burial likely had $\delta^{18}O_{\_VSMOW}$ values (Fig. 16B) heavier than Early Triassic normal

seawater (−1 ‰), assuming that the Early Triassic planet was ice-free and coeval shallow water ranged from 32 to 38 °C (Sun et al., 2012).

Dolomite formed in near-surface and shallow burial environments commonly has poorly ordered, metastable phases (i.e., protodolomite) that are thermodynamically unstable when temperature, pressure, and fluid composition change (Gregg et al., 2015; Kaczmarek et al., 2017; Machel, 2004; Ren and Jones, 2018). During replacement, the textural and geochemical signatures of early, metastable dolomite can be

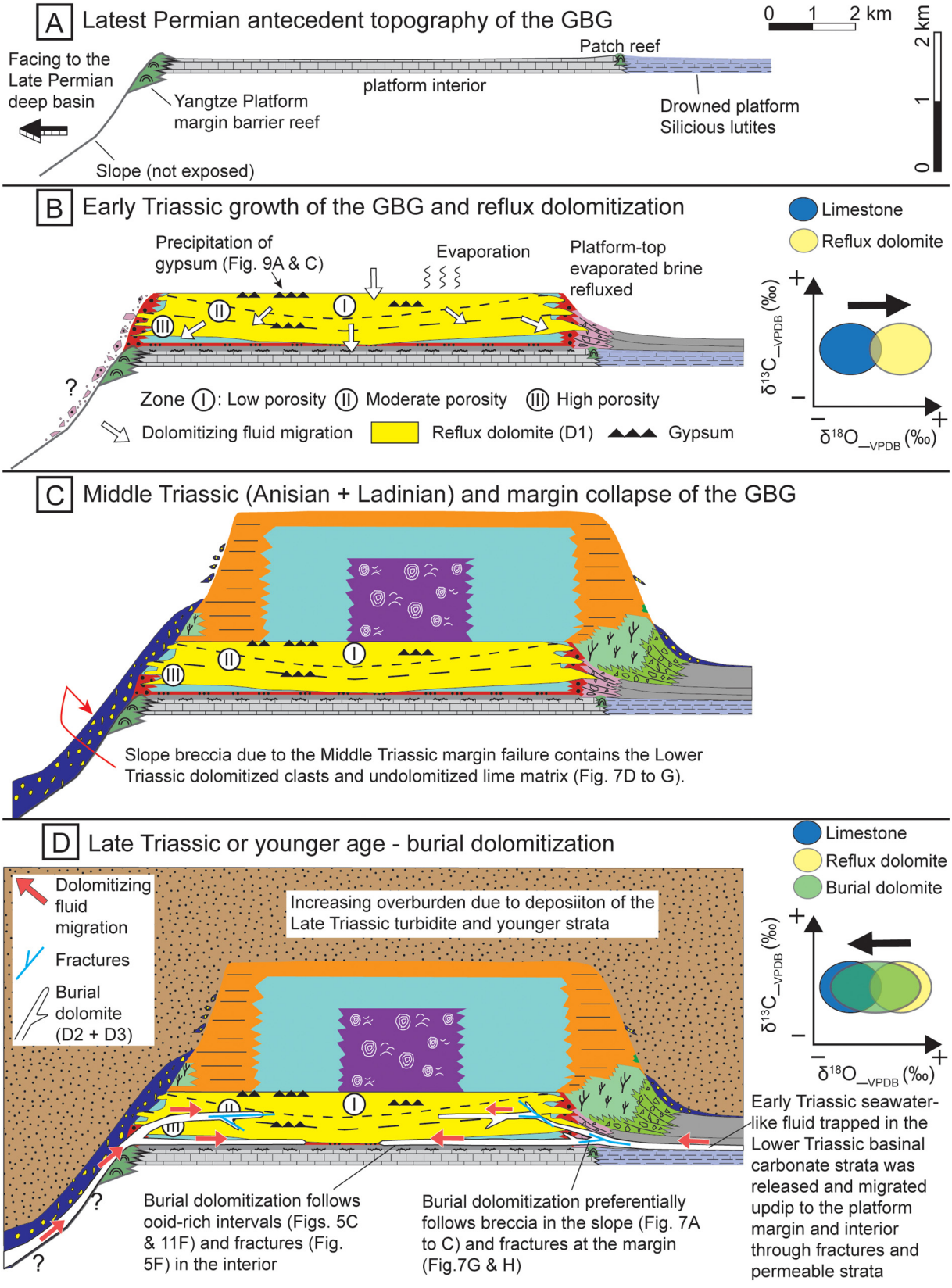

partially or entirely overprinted. D1 was locally replaced during reaction with late burial fluid. Flow of late-burial fluid towards the platform interior on the GBG is indicated by the presence of high-temperature D2 and D3 in ooidal molds and along fractures (Figs. 5F and 11F) in the platform interior strata where D1 was initially formed. During precipitation of carbonate minerals from normal seawater, distribution coefficients control Sr and Mn concentrations in carbonate minerals, driving Sr-enriched and Mn-depleted calcite or aragonite (Banner, 1995). The distribution coefficient for Sr in dolomite ranges from 0.039 to 0.048 (Banner, 1995), approximately half the corresponding value in calcite (Banner, 1995; Vahrenkamp and Swart, 1990). In contrast, the distribution coefficient of Mn in dolomite is >1 (Vahrenkamp and Swart, 1990). Therefore, more Sr ions are apt to stay in diagenetic fluid, whereas more Mn ions tend to be incorporated into crystal lattice during recrystallization of dolomite and dolomite replacement of calcite (Banner, 1995). During progressive dolomite recrystallization or dolomite replacement of calcite in the burial stage, Sr concentrations in dolomite and calcite tend to decrease while Sr concentrations increase in diagenetic fluids, so more Sr ions are likely to enter dolomite that formed late (Banner, 1995). Consequently, dolomite that formed due to the same formation mechanism (D2 and D3) but in different time probably explains the wide range of Sr and Mn for D2 and D3 (Fig. 15B).

Carbon and oxygen isotopic variations in the same system can be used as a preliminary tool to analyze water-rock interaction. Water-rock ratios required for carbonate minerals to be reset and equilibrate with fluid $\delta^{18}O$ values are at least two orders of magnitude lower (<10) than the water-rock ratios at which they are in equilibrium with fluid $\delta^{13}C$ values (10^3; Banner and Hanson, 1990). $\delta^{13}C$ values of dolomite in this study (Fig. 16A) are consistent with the $\delta^{13}C$ range of the Lower Triassic marine carbonates (Payne et al., 2004). This consistency implies that dolomitizing fluid responsible for the formation of D2 and D3 likely did not need to have a great volume to equilibrate with the Early Triassic limestone or dolomite (D1) and that it was a rock-dominated system when the late burial-compaction dolomitization occurred. This indication of a relatively small volume of dolomitizing fluid also suggests that burial dolomite, in contrast to early reflux dolomite, plays a secondary role in forming the studied dolostone interval. Its secondary role is consistent with field observations where burial dolomite of high Th locally occurs along fractures in the platform interior and slope (Figs. 5F and 7H) rather than pervasively and extensively replaces the platform interior. The scope of $\delta^{18}O$ values of D2 and D3 overlaps with those of host limestone and D1 (p-value = 0.21 according to ANOVA), suggesting that burial dolomitizing fluid likely did not interact extensively with the host limestone and D1; and the water-rock ratios during dolomitization were relatively low. Therefore, the measured $\delta^{18}O$ values of D2 and D3 probably retain the geochemical attributes of the host limestone and reflux dolomite (D1). This scenario also explains the why the scopes of isotopic and trace element compositions of limestone and different types of dolomite generally overlap (Fig. 16A).

5.5. Conceptual model

Seawater dolomitization induced by geothermal convection has been interpreted for extensive dolostone in carbonate islands (Budd, 1997; Ren and Jones, 2018; Wang et al., 2019; Whitaker et al., 1994). However, a few patterns predicted from the seawater dolomitization model induced by geothermal convection (Ren and Jones, 2018; Wang et al., 2019) do not occur or even show contradictory trends at the GBG. For example, $\delta^{13}C$ at the GBG is conversely more depleted in slope and basinal facies and heavier in the interior (Kelley et al., 2020; Meyer et al., 2011). Furthermore, the dolostone strata at the GBG do not thin from the platform margin to the interior. Moreover, fabric-retentive and fabric-destructive fabrics could be preserved in the same strata (e.g., Fig. 6B), and there is no overall trend from fabric-retentive to fabric-destructive textures from the margin to interior at the GBG.

In Holocene marine and coastal lagoon environments, finely crystalline dolomite mediated by microbial activity can form directly from seawater in association with bacterial removal of sulfate and related increase of magnesium ions in the water (Bontognali et al., 2010; Sánchez-Román et al., 2008, 2009; Teal et al., 2000; Vasconcelos and Mckenzie, 1997). Magnesium ions in the synsedimentary dolomite are moved through diffusion rather than advection. In modern environments this process yields only small amounts of stratiform dolomite. Therefore, this microbial model is also not sufficient to account for the thick succession of massive dolostone in the studied area.

In addition, fault-controlled hydrothermal dolomitization is commonly thought to form from magnesium-rich fluids that originate from a deep over-pressured aquifer and migrate via normal or strike-slip faults under burial environment and can form dolomite cement and replacive dolomite (Hendry et al., 2015). However, fault conduits are not developed in the studied transect (Figs. 2B and 3), so fault-controlled hydrothermal dolomitization is not supported as a likely model to account for the massive dolostone in the GBG.

Therefore, an integrated model involving early evaporation seepage-reflux dolomitization (D1) overprinted by subsequent burial-compaction dolomitization (D2 and D3) is proposed in this study (Fig. 19; Table 1). D1, generally thinning from the platform interior to the slope (Fig. 4), cross-cutting bedding planes (Fig. 6F), being preserved together with gypsum (Fig. 9C), and showing similar $^{87}Sr/^{86}Sr$ values of the Early Triassic seawater (Fig. 17), in conjunction with dolomitized clasts of microbialite, fenestral limestone, oolite and undolomitized micrite in slope lime breccia (Figs. 7D to F, 19B and C), indicates that Early Triassic refluxing dolomitizing fluids moved through the platform interior and margin sediments shortly after deposition but prior to transport of the dolomitized clasts to the slope and deep burial of the platform in the Middle Triassic (Lehrmann et al., 2020). D1 is interpreted to result from evaporation seepage-reflux dolomitization. Kaufman (1994) and Warren (2000) suggest that position and spatial thickness variations of dolomite within a basin can indicate migration pathways of dolomitizing fluid. The accumulative thickness of massive dolostone thinning from the platform interior to basin margin (Fig. 4) indicates that the dolomitizing fluid predominantly originated from platform top and migrated through permeable conduits to the platform margin and slope (Garcia-Fresca et al., 2012; Wang et al., 2015).

Deep burial-compaction dolomitization (D2 and D3) is interpreted to have occurred during or later than the Late Triassic Carnian, when Early Triassic seawater-like fluid that was trapped in the adjacent Lower Triassic basinal carbonate sediments was expelled by compaction

Fig. 19. An integrated model showing reflux dolomitization overprinted by burial-compaction dolomitization. (A) Latest Permian antecedent topography for the initial growth of the GBG. (B) Reflux dolomitization responsible for the formation of dolomite type 1. Evaporites precipitated out of the platform-top evaporated seawater. Early Triassic evaporated seawater on the platform top cross-cut and refluxed the platform interior and the margin. Initial dolomitization of limestone by evaporated seawater leads to dolomite type 1 with substantial porosity (Zone III). Evaporated seawater flowing through previously dolomitized areas continues to decrease porosity by precipitation of additional dolomite (Zones II and I). Reflux dolomitization drives dolomite to be enriched in ^{18}O relative to the host limestone. The relatively low $\delta^{18}O$ values of D1 likely suggest that pristine values had been reset to be ^{16}O-enriched due to geothermal heating after the GBG was buried by marine turbidites. (C) Early Triassic dolomitized fabrics at the interior and margin (e.g., microbialite, fenestral limestone, and oolite) were transported to slope due to margin failure in the Middle Triassic. The resultant slope breccia contains dolomitized clasts and undolomitized lime mud (Fig. 7D to G). (D) Early Triassic dolomite type 1 are overprinted by following burial dolomitization related to Early Triassic seawater-like fluid that was expelled from the Lower Triassic basinal carbonate sediments and migrated updip to the margin and interior through fractures and permeable strata. The burial dolomitization occurred during or later than the Late Triassic. Water-rock interactions during burial probably replaces and resets local host limestone and dolomite type 1, and also drives depletion of ^{18}O in dolomite type 2 and 3 relative to dolomite type 1 and host limestone, and it leads to geochemical overlapping of host limestone and different types of dolomite. Legend symbols in Fig. 19 are the same as in Fig. 3. (For interpretation of the references to colour in this figure legend, the reader is referred to the web version of this article.)

and then migrated through the platform strata along permeable strata and fractures at the slope, margin, and interior (Fig. 19D). D2 and D3 have been also recognized in samples collected from the platform interior, margin, slope, and basin margin. Evidence for a late-stage, deep-burial origin includes tannish dolomitization fronts that follow fractures, hot dolomitizing fluid indicated by high T_h range of fluid inclusions in D2 and D3, along with fluid inclusion data indicating a wide range of salinities from brackish water to saltier than normal seawater (Figs. 13 and 14). Similar compaction-driven dolomitization has also been interpreted by Reinhold (1998), Saller and Dickson (2011), and Wang et al. (2015). Moreover, dolomitization of the slope, characterized by coarser dolomite crystals and common occurrences of D2 and D3 with undulatory extinction, preferentially following clast-supported lime breccia at the northern margin of the GBG (Fig. 7A to C), is also consistent with a burial-compaction origin supported by numerical simulation results. Reactive transport modeling of dolomitization indicates that in near-surface environments, magnesium-rich fluid prefers to dolomitize more reactive micrite-rich sediments in which permeability allows flow of magnesium-rich fluid. In contrast, reactions would be favorably focused in more permeable but less reactive grainy sediments in burial environments where flow rates decrease (Al-Helal et al., 2012).

Initial dolomitization of the platform interior carbonate deposit by evaporated seawater generates dolomite with porosity, and the extent of reflux dolomitization generally wanes along the flow pathway from the top of the platform (Zones I to III in Fig. 19B). Two examples are from the carbonate platforms in the Permian basin and Arkoma basin (Saller, 2004; Wahlman, 2010). However, as dolomitization continues, additional flow results in precipitation of extra dolomite (over-dolomitization) that decreases or even blocks early-formed porosity near its proximal end to the evaporated seawater, whereas its distal end could still retain pores (Saller, 2004; Wahlman, 2010; Zones I to III in Fig. 19B). The resultant spatial variations of porosity likely explain the spatial variation trend of preserved porosity identified from thin sections (<1 % in the platform interior versus 1 % to 6 % at the margin). Burial dolomitization characterized by coarser D2 and D3 took place at the distal end, such as slope and basin margin breccia, where the greater porosity and permeability after early reflux dolomitization are still suitable for burial dolomitizing fluid to escape (Fig. 19B). However, progressive burial dolomitization could also lead to over-dolomitization that decreases or entirely blocks early-formed porosity near its proximal end to the basinal brine, whereas its distal end to the platform margin could still retain pores (Koeshidayatullah et al., 2020; Fig. 19D). The low porosity in the platform interior after early reflux dolomitization constrain the volume of burial dolostone (~40 m thick at slope in Fig. 4) to be smaller than early reflux dolostone in the Lower Triassic strata. Moreover, they explain petrographic observations that D2 and D3 are more abundant on the slope and basin margin than in the platform interior.

In addition, the original isotope composition of Early Triassic seawater-like fluids trapped in the Lower Triassic basinal carbonate sediments would have been altered by water-rock interactions during burial that drove depletion of ^{18}O in the dolomite minerals and enrichment in the fluid (Land, 1980). Evaporation results in enrichment of ^{18}O in the platform top seawater, and $\delta^{18}O$ of the resultant seepage-reflux dolomite would be more positive than coeval host limestone (Fig. 19B). The early evaporation and following burial processes altered $\delta^{18}O$ in opposite direction (Fig. 19B and D), providing a reasonable explanation for the observed overlapping ranges of $\delta^{18}O$ of the Early Triassic host limestone, D1, D2, and D3 (ANOVA p -$value$ = 0.21; Fig. 16A).

This study illustrates potentially effective avenues for unraveling two dolomitization mechanisms operating within the same carbonate platform. Petrographic evidence in the slope of the GBG (i.e., dolomitized clasts in slope lime breccia in Table 1 and Fig. 7D to G) is a key to determining whether subsequent burial dolomitization can be distinguished from early reflux dolomitization within the dolostone body in the study area. Slope deposits are far from sources of Early Triassic platform-top brine and are therefore less likely to be pervasively dolomitized if over-dolomitization occurs in the area proximal to the evaporated brine (Whitaker and Xiao, 2010). If the slope is only partially dolomitized during initial burial, the slope may be the facies most likely to preserve petrographic evidence of otherwise overprinted dolomitization mechanisms. Moreover, D1 retains its Early Triassic seawater $\delta^{13}C$ and $^{87}Sr/^{86}Sr$ signatures (Figs. 16A and 17). Isotopic (e.g., $\delta^{18}O$) and elemental proxy data are likely to be altered from primary (or even secondary) values when a late dolomitization mechanism overprints an early different one, with the outcome depending on the degree to which the proxy behaves as rock-buffered versus fluid-buffered system. This suggests that the same dolomite archive may retain well-preserved or altered data depending on the analyzed geochemical proxy.

5.6. Future work

Conventional approaches applied in this study could separate some, but not all, signatures of the two different dolomitization mechanisms (Table 1). A key remaining challenge for estimating the 3-D volume of reflux versus burial dolostone in the GBG is determining the contact between reflux dolostone and burial dolostone across the studied 2-D transect along the Bianyang syncline (Fig. 19D). Accomplishing this goal will further make it possible to estimate the 3-D volume of dolostone of the two separate mechanisms in the whole GBG if spatial thickness variations of dolostone are known from the Bianyang syncline eastwards to the Xiliang syncline (Fig. 2B). Moreover, estimating the volume of burial dolomitizing fluids required to form D2 and D3 will then be possible. In addition, it will help understand how burial dolomitizing fluids overprint and reset geochemical properties of reflux dolostone in combination with reactive transport modeling. Application of new techniques with high spatial resolution for in situ measurement (Nano-SIMS for thermometry and in situ isotopic and elemental analysis; Denny et al., 2020) in conjunction with XRD analysis for stoichiometry of dolomite crystals is likely the solution to the challenge (Manche and Kaczmarek, 2019). The new techniques can (1) help understand $\delta^{18}O$ variations of dolomite at a nanoscopic scale, (2) correlate the $\delta^{18}O$ to each measured temperature and stoichiometry of reflux versus burial dolomite in order to further distinguish the formation mechanisms of separate petrographic phases and reconstructing the overprinting process of the two dolomitization mechanisms.

6. Summary and conclusions

Massive dolostone forms via multiple, successive mechanisms. Whether later dolomitization mechanisms can be distinguished from early ones within a given dolostone body depends on whether evidence of early-formed dolomite is still detectable by conventional approaches. This study assesses different mechanisms contributing to the underexplored massive dolostone in the Lower Triassic strata of the GBG in the Nanpanjiang Basin. The Lower Triassic dolostone of the GBG comprises three dolomite phases. Dolomite type 1 formed due to the reflux of Early Triassic evaporated seawater that had reached gypsum saturation on the platform top and flowed through the platform interior facies. Dolomite types 2 and 3 formed in a deep burial environment and played a secondary role in forming the Lower Triassic massive dolostone. The dolomitizing fluid that resulted in the formation of dolomite types 2 and 3 was mainly derived from Early Triassic seawater-like fluid. The Early Triassic seawater-like fluid was expelled from the Lower Triassic basinal carbonate sediments and flowed updip to the platform margin and platform interior where porosity and permeability was suitable for the fluid to migrate during or after the Late Triassic. These findings suggest that dolomitized clasts in slope lime breccia can be particularly important for distinguishing early reflux dolomitization from later burial dolomitization and, more generally, that the slope facies is a

promising area for preservation of field and petrographic evidence to distinguish among dolomitization mechanisms.

Dolomite type 1 retains its Early Triassic seawater $\delta^{13}C$ and $^{87}Sr/^{86}Sr$ signatures (Figs. 16A and 17). Overlapping geochemical fields of the three types of dolomite implies that burial dolomitizing fluids in equilibrium with dolomite types 2 and 3 locally reset the geochemistry of the dolomite type 1 that formed the majority of the massive dolostone in the platform interior and margin. Oxygen isotopic or elemental proxy data have the potential to be reset when a late burial dolomitization overprints the early dolomite, with the outcome depending on fluid composition and whether the overprinting process acts as a fluid-buffered or rock-buffered system. This finding suggests that the same dolomite archive may retain well-preserved or altered data depending on which geochemical proxies are analyzed and that multiple field, petrographic, geothermometric, and geochemical data should be integrated in assessment of dolomitization mechanisms rather than relying only on geochemical proxies.

Declaration of competing interest

The authors declare that they have no known competing financial interests or personal relationships that could have appeared to influence the work reported in this paper.

Acknowledgements

We acknowledge Dale Burns, David Mucciarone, and Karrie Weaver for laboratory assistance with geochemical analyses at Stanford University; Nathaniel Adams, Leanne Stepchinski, Dongyang Liu, Qiushi Ning, and Ji Li for field assistance; Jiayong Wei and Paul Enos for their support to our Triassic geological research in Guizhou Province. This study was partially supported via funding from Shell (PT31819) and Aramco (6500011100) grants to Payne and Lehrmann, and the American Chemical Society Petroleum Research Fund grants (45329-G8 to Payne and 53075-UR8 to Lehrmann). Continued collaborative work on this project has been supported by NSF grants (EAR 204315 and 204316) to Lehrmann and Luczaj. Li appreciates extra support from the IAS Postgraduate Research Grant, the AAPG Foundation J. E. Kilkenny Memorial Grant, and the Stanford University McGee-Levorsen Research Grant for sponsoring part of the analyses and travel expenses. We thank Journal Manager Parthiban Rajendran for handling the manuscript; Editor Massimo Moretti and two anonymous reviewers whose constructive comments help improved the clarity of the paper.

Appendix A. Supplementary data

Supplementary data to this article can be found online at https://doi.org/10.1016/j.sedgeo.2022.106240.

References

Adams, J.E., Rhodes, M.L., 1960. Dolomitization by seepage refluxion. AAPG Bulletin 44, 1912–1920. https://doi.org/10.1306/bc74368d-16be-11d7-8645000102c1865d.

Al-Awwad, S.F., Collins, L.B., 2013. Arabian carbonate reservoirs: a depositional model of the Arab-D reservoir in Khurais field, Saudi Arabia. AAPG Bulletin 97, 1099–1119. https://doi.org/10.1306/11051212103.

Al-Helal, A.B., Whitaker, F.F., Xiao, Y., 2012. Reactive transport modeling of brine reflux: dolomitization, anhydrite precipitation, and porosity evolution. Journal of Sedimentary Research 82, 196–215. https://doi.org/10.2110/jsr.2012.14.

Amel, H., Jafarian, A., Husinec, A., Koeshidayatullah, A., Swennen, R., 2015. Microfacies, depositional environment and diagenetic evolution controls on the reservoir quality of the Permian Upper Dalan Formation, Kish Gas Field, Zagros Basin. Marine and Petroleum Geology 67, 57–71. https://doi.org/10.1016/j.marpetgeo.2015.04.012.

Banner, J.L., 1995. Application of the trace element and isotope geochemistry of strontium to studies of carbonate diagenesis. Sedimentology 42, 805–824. https://doi.org/10.1111/j.1365-3091.1995.tb00410.x.

Banner, J.L., Hanson, G.N., 1990. Calculation of simultaneous isotopic and trace element variations during water-rock interaction with applications to carbonate diagenesis. Geochimica et Cosmochimica Acta 54, 3123–3137. https://doi.org/10.1016/0016-7037(90)90128-8.

Barnaby, R.J., Read, J.F., 1992. Dolomitization of a carbonate platform during late burial: Lower to Middle Cambrian Shady dolomite, Virginia Appalachians. Journal of Sedimentary Petrology 62, 1023–1043. https://doi.org/10.1306/D4267A3C-2B26-11D7-8648000102C1865D.

Bodnar, R.J., 1993. Revised equation and table for determining the freezing point depression of H2O-NaCl solutions. Geochimica et Cosmochimica Acta 57, 683–684. https://doi.org/10.1016/0016-7037(93)90378-A.

Bontognali, T.R.R., Vasconcelos, C., Warthmann, R., Bernasconi, S.M., Dupraz, C., Strohmenger, C.J., Mckenzie, J.A., 2010. Dolomite formation within microbial mats in the coastal sabkha of Abu Dhabi (United Arab Emirates). Sedimentology 57, 824–844. https://doi.org/10.1111/j.1365-3091.2009.01121.x.

Budd, D.A., 1997. Cenozoic dolomites of carbonate islands: their attributes and origin. Earth-Science Reviews 42, 1–47. https://doi.org/10.1016/S0012-8252(96)00051-7.

Chatalov, A., 2013. Flowchart for micropetrographic description and classification of dolostones. Carbonates and Evaporites 28, 447–456. https://doi.org/10.1007/s13146-013-0140-y.

Davies, G.R., Smith Jr., L.B., 2006. Structurally controlled hydrothermal dolomite reservoir facies : an overview. AAPG Bulletin 90, 1641–1690. https://doi.org/10.1306/05220605164.

Denny, A.C., Orland, I.J., Valley, J.W., 2020. Regionally correlated oxygen and carbon isotope zonation in diagenetic carbonates of the Bakken Formation. Chemical Geology 531, 119327. https://doi.org/10.1016/j.chemgeo.2019.119327.

Dong, Y., Chen, H., Wang, J., Hou, M., Xu, S., Zhu, P., Zhang, C., Cui, Y., 2020. Thermal convection dolomitization induced by the Emeishan large Igneous Province. Marine and Petroleum Geology 116, 104308. https://doi.org/10.1016/j.marpetgeo.2020.104308.

Dravis, J.J., Wanless, H.R., 2018. Reflux dolomitization – a Holocene example beneath a coastal salina, West Caicos Island, Turks and Caicos Islands. Marine and Petroleum Geology 97, 311–322. https://doi.org/10.1016/j.marpetgeo.2018.07.003.

Edwards, C.T., Saltzman, M.R., Leslie, S.A., Bergström, S.M., Sedlacek, A.R.C., Howard, A., Bauer, J.A., Sweet, W.C., Young, S.A., 2015. Strontium isotope (87Sr/86Sr) stratigraphy of Ordovician bulk carbonate: implications for preservation of primary seawater values. Bulletin of the Geological Society of America 127, 1275–1289. https://doi.org/10.1130/B31149.1.

Ehrenberg, S.N., Nadeau, P.H., Agrawi, A.A.M., 2007. A comparison of Khuff and Arab reservoir potential throughout the Middle East. AAPG Bulletin 91, 275–286. https://doi.org/10.1306/09140606054.

Enos, P., Lehrmann, D.J., Wei, J., Yu, Y., Xiao, J., Chaikin, D.H., Minzoni, M., Berry, A.K., Montgomery, P., 2006. Triassic Evolution of the Yangtze Platform in Guizhou Province, People's Republic of China. Geological Society of America Special Papervol. 417.

Faure, G., Powell, J.L., 1972. Strontium Isotope Geology. Springer.

Garaguly, I., Varga, A., Raucsik, B., Schubert, F., Czuppon, G., Frei, R., 2018. Pervasive early diagenetic dolomitization, subsequent hydrothermal alteration, and late stage hydrocarbon accumulation in a Middle Triassic carbonate sequence (Szeged Basin, SE Hungary). Marine and Petroleum Geology 98, 270–290. https://doi.org/10.1016/j.marpetgeo.2018.07.024.

Garcia-Fresca, B., Jerry Lucia, F., Sharp, J.M., Kerans, C., 2012. Outcrop-constrained hydrogeological simulations of brine reflux and early dolomitization of the Permian San Andres Formation. AAPG Bulletin 96, 1757–1781. https://doi.org/10.1306/02071210123.

Goldstein, R.H., Reynolds, T.J., 1994. Systematics of Fluid Inclusions in Diagenetic Minerals: SEPM Short Course 31. Society for Sedimentary Geology https://doi.org/10.2110/scn.94.31.

Gregg, J.M., Bish, D.L., Kaczmarek, S.E., Machel, H.G., 2015. Mineralogy, nucleation and growth of dolomite in the laboratory and sedimentary environment: a review. Sedimentology 1749–1769. https://doi.org/10.1111/sed.12202.

Haas, J., Budai, T., Gyori, O., Kele, S., 2014. Multiphase partial and selective dolomitization of Carnian reef limestone (Transdanubian Range, Hungary). Sedimentology 61, 836–859. https://doi.org/10.1111/sed.12088.

Hendry, J.P., Gregg, J.M., Shelton, K.L., Somerville, I.D., Crowley, S.F., 2015. Origin, characteristics and distribution of fault-related and fracture-related dolomitization: insights from Mississippian carbonates, Isle of Man. Sedimentology 62, 717–752. https://doi.org/10.1111/sed.12160.

Horita, J., 2014. Oxygen and carbon isotope fractionation in the system dolomite-water-CO2 to elevated temperatures. Geochimica et Cosmochimica Acta 129, 111–124. https://doi.org/10.1016/j.gca.2013.12.027.

Jackson, M.G., Hart, S.R., 2006. Strontium isotopes in melt inclusions from Samoan basalts: implications for heterogeneity in the Samoan plume. Earth and Planetary Science Letters 245, 260–277. https://doi.org/10.1016/j.epsl.2006.02.040.

Jiang, L., Worden, R., Cai, C., Li, K., Xiang, L., Cai, L., He, X., 2014. Dolomitization of gas reservoirs: the Upper Permian Changxing and Lower Triassic Feixianguan Formations, Northeast Sichuan Basin, China. Journal of Sedimentary Research 84, 792–815. https://doi.org/10.2110/jsr.2014.65.

Jiang, L., Worden, R.H., Cai, C.F., Shen, A.J., He, X.Y., Pan, L.Y., 2018. Contrasting diagenetic evolution patterns of platform margin limestones and dolostones in the Lower Triassic Feixianguan Formation, Sichuan Basin, China. Marine and Petroleum Geology 92, 332–351. https://doi.org/10.1016/j.marpetgeo.2017.10.029.

Kaczmarek, S.E., Gregg, J.M., Bish, D.L., Machel, H.G., Fouke, B.W., 2017. Dolomite, very high-magnesium calcite, and microbes - implications for the microbial model of dolomitization. In: MacNeil, A.J., Jeff, L., Rachel, W. (Eds.), Characterization and Modeling of Carbonates–Mountjoy Symposium 1. SEPM Special Publicationvol. 109, pp. 1–14. https://doi.org/10.2110/sepmsp.109.01.

Kaufman, J., 1994. Numerical models of fluid flow in carbonate platforms: implications for dolomitization. Journal of Sedimentary Research A64, 128–139. https://doi.org/10.1306/D4267D2F-2B26-11D7-8648000102C1865D.

Kaufman, A.J., Knoll, A.H., 1995. Neoproterozoic variations in the C-isotopic composition of seawater: stratigraphic and biogeochemical implications. Precambrian Research 73, 27–49. https://doi.org/10.1016/0301-9268(94)00070-8.

Kelley, B.M., Lehrmann, D.J., Yu, M., Jost, A.B., Meyer, K.M., Lau, K.V., Altiner, D., LI, X., Minzoni, M., Schaal, E.K., Payne, J.L., 2020. Controls on carbonate platform architecture and reef recovery across the Palaeozoic to Mesozoic transition: a high-resolution analysis of the Great Bank of Guizhou. Sedimentology 67, 3119–3151. https://doi.org/10.1111/SED.12741.

Koeshidayatullah, A., Corlett, H., Stacey, J., Swart, P.K., Boyce, A., Hollis, C., 2020. Origin and evolution of fault-controlled hydrothermal dolomitization fronts : a new insight. Earth and Planetary Science Letters 541 (1−13), 116291. https://doi.org/10.1016/j.epsl.2020.116291.

Korte, C., Kozur, H.W., Bruckschen, P., Veizer, J., 2003. Strontium isotope evolution of Late Permian and Triassic seawater. Geochimica et Cosmochimica Acta 67, 47–62. https://doi.org/10.1016/S0016-7037(02)01035-9.

Land, L.S., 1980. The isotopic and trace element geochemistry of dolomite: the state of the art. In: Zenger, D.H., Dunham, J.B., Ethington, R.L. (Eds.), Concepts and Models of Dolomitization. SEPM Special Publicationvol. 28, pp. 87–110.

Land, L.S., 1998. Failure to precipitate dolomite at 25°C from dilute solution despite 1000-fold oversaturation after 32 years. Aquatic Geochemistry 4, 361–368. https://doi.org/10.1023/A:1009688315854.

Lehrmann, D.J., Jiayong, Wei, Enos, P., 1998. Controls on facies architecture of a large Triassic carbonate platform: the Great Bank of Guizhou, Nanpanjiang Basin, south China. Journal of Sedimentary Research 68, 311–326. https://doi.org/10.2110/jsr.68.311.

Lehrmann, D.J., Donghong, P., Enos, P., Minzoni, M., Ellwood, B.B., Orchard, M.J., Jiyan, Z., Jiayong, W., Dillett, P., Koening, J., Steffen, K., Druke, D., Druke, J., Kessel, B., Newkirk, T., 2007. Impact of differential tectonic subsidence on isolated carbonate-platform evolution: Triassic of the Nanpanjiang Basin, south China. AAPG Bulletin 91, 287–320. https://doi.org/10.1306/10160606065.

Lehrmann, D.J., Minzoni, M., Li, X., Yu, M., Payne, J.L., Kelley, B.M., Schaal, E.K., Enos, P., 2012. Lower Triassic oolites of the Nanpanjiang Basin, south China: facies architecture, giant ooids, and diagenesis-implications for hydrocarbon reservoirs. AAPG Bulletin 96, 1389–1414. https://doi.org/10.1306/01231211148.

Lehrmann, D.J., Chaikin, D.H., Enos, P., Minzoni, M., Payne, J.L., Yu, M., Goers, A., Wood, T., Richter, P., Kelley, B.M., Li, X., Qin, Y., Liu, L., Lu, G., 2015. Patterns of basin fill in Triassic turbidites of the Nanpanjiang basin: implications for regional tectonics and impacts on carbonate-platform evolution. Basin Research 27, 587–612. https://doi.org/10.1111/bre.12090.

Lehrmann, D.J., Minzoni, M., Enos, P., Kelleher, C., Stepchinski, L., Li, X., Payne, J.L., Yu, M., 2020. Giant sector-collapse structures (scalloped margins) of the Yangtze Platform and Great Bank of Guizhou, China: Implications for genesis of collapsed carbonate platform margin systems. Sedimentology 67, 3167–3198. https://doi.org/10.1111/sed.12740.

Li, X., Yu, M., Lehrmann, D.J., Payne, J.L., Kelley, B.M., Minzoni, M., 2012. Factors controlling carbonate platform asymmetry: preliminary results from the Great Bank of Guizhou, an isolated Permian-Triassic Platform in the Nanpanjiang Basin, south China. Palaeogeography, Palaeoclimatology, Palaeoecology 315–316, 158–171. https://doi.org/10.1016/j.palaeo.2011.11.023.

Li, X., Falivene, O., Minzoni, M., Lehrmann, D.J., Reijmer, J.J.G., Morsilli, M., Al-ramadan, K.A.H., Yu, M., Payne, J.L., 2020. Interactions between sediment production and transport in the geometry of carbonate platforms: insights from forward modeling of the Great Bank of Guizhou (Early to Middle Triassic), south China. Marine and Petroleum Geology 118, 104416. https://doi.org/10.1016/j.marpetgeo.2020.104416.

Li, X., Trower, E.J., Lehrmann, D.J., Minzoni, M., Kelley, B.M., Schaal, E.K., Altiner, D., Yu, M., Payne, J.L., 2021. Implications of giant ooids for the carbonate chemistry of Early Triassic seawater. Geology 49, 156–161. https://doi.org/10.1130/G47655.1.

Machel, H., 2004. Concepts and models of dolomitization: a critical reappraisal. In: Braithwaite, C.J.R., Rizzi, G., Dark, G. (Eds.), The Geometry and Petrogenesis of Dolomite Hydrocarbon ReservoirsGeological Society of London Special Publicationsvol. 235, pp. 7–63. https://doi.org/10.1144/GSL.SP.2004.235.01.02.

Machel, H.G., Anderson, J.H., 1989. Pervasive subsurface dolomitization of the Nisku Formation in central Alberta. Journal of Sedimentary Research 59, 891–911. https://doi.org/10.1306/212F90AC-2B24-11D7-8648000102C1865D.

Manche, C.J., Kaczmarek, S.E., 2019. Evaluating reflux dolomitization using a novel high-resolution record of dolomite stoichiometry: a case study from the Cretaceous of central Texas, USA. Geology 47, 586–590. https://doi.org/10.1130/G46218.1.

Martin, E.E., Macdougall, J.D., 1995. Sr and Nd isotopes at the Permian/Triassic boundary: a record of climate change. Chemical Geology 125, 73–99. https://doi.org/10.1016/0009-2541(95)00081-V.

McArthur, J.M., Howarth, R.J., Bailey, T.R., 2001. Strontium isotope stratigraphy: LOWESS Version 3: best fit to the marine Sr-isotope curve for 0-509 Ma and accompanying look-up table for deriving numerical age. The Journal of Geology 109, 155–170. https://doi.org/10.1086/319243.

Meyer, K.M., Yu, M., Jost, A.B., Kelley, B.M., Payne, J.L., 2011. δ13C evidence that high primary productivity delayed recovery from end-Permian mass extinction. Earth and Planetary Science Letters 302, 378–384. https://doi.org/10.1016/j.epsl.2010.12.033.

Minzoni, M., Lehrmann, D.J., Payne, J., Enos, P., Yu, M., Wei, J., Kelley, B., Li, X., Schaal, E., Meyer, K., Montgomery, P., Goers, A., Wood, T., 2014. Triassic tank: platform margin and slope architecture in space and time, Nanpanjiang Basin, south China. In: Verwer, K., Playton, T.E., Harris, P.M., Mitch (Eds.), Deposits, Architecture, and Controls of Carbonate Margin, Slope and Basinal Settings. SEPM Special Publicationvol. 105, pp. 84–113. https://doi.org/10.2110/sepmsp.105.10.

Nader, F.H., Swennen, R., Ellam, R., 2004. Reflux stratabound dolostone and hydrothermal volcanism-associated dolostone: a two-state dolomitization model (Jurassic, Lebanon). Sedimentology 51, 339–360. https://doi.org/10.1111/j.1365-3091.2004.00629.x.

Payne, J.L., Lehrmann, D.J., Wei, J., Orchard, M.J., Schrag, D.P., Knoll, A.H., 2004. Large perturbations of the carbon cycle during recovery from the End-Permian extinction. Science 305, 506–509. https://doi.org/10.1126/science.1097023.

Reinhold, C., 1998. Multiple episodes of dolomitization and dolomite recrystallization during shallow burial in Upper Jurassic shelf carbonates: eastern Swabian Alb, southern Germany. Sedimentary Geology 121, 71–95. https://doi.org/10.1016/S0037-0738(98)00077-3.

Ren, M., Jones, B., 2018. Genesis of island dolostones. Sedimentology 65, 2003–2033. https://doi.org/10.1111/sed.12455.

Ronchi, P., Jadoul, F., Ceriani, A., Di Giulio, A., Scotti, P., Ortenzi, A., Previde Massara, E., 2011. Multistage dolomitization and distribution of dolomitized bodies in Early Jurassic carbonate platforms (Southern Alps, Italy). Sedimentology 58, 532–565. https://doi.org/10.1111/j.1365-3091.2010.01174.x.

Saller, A.H., 2004. Palaeozoic dolomite reservoirs in the Permian Basin, SW USA: stratigraphic distribution, porosity, permeability and production. In: Braithwaite, C.J.R., Rizzi, G., Dark, G. (Eds.), The Geometry and Petrogenesis of Dolomite Hydrocarbon Reservoirs. Geological Society of London Special Publicationsvol. 235, pp. 309–323. https://doi.org/10.1144/GSL.SP.2004.235.01.13.

Saller, A.H., Dickson, J.A.T.D., 2011. Partial dolomitization of a Pennsylvanian limestone buildup by hydrothermal fluids and its effect on reservoir quality and performance. AAPG Bulletin 95, 1745–1762. https://doi.org/10.1306/02141110117.

Sánchez-Román, M., Vasconcelos, C., Schmid, T., Dittrich, M., McKenzie, J.A., Zenobi, R., Rivadeneyra, M.A., 2008. Aerobic microbial dolomite at the nanometer scale: implications for the geologic record. Geology 36, 879–882. https://doi.org/10.1130/G25013A.1.

Sánchez-Román, M., Vasconcelos, C., Warthmann, R., Rivadeneyra, M., McKenzie, Judith A., 2009. Microbial dolomite precipitation under aerobic conditions: results from Brejo do Espinho Lagoon (Brazil) and culture experiments. In: Swart, P.K., Eberli, G. P., McKenzie, J.A. (Eds.), Perspectives in Sedimentary Geology: A Tribute to the Career of Robert Nathan Ginsburg. vol. 41. IAS Special Publication, pp. 167–178.

Schoenherr, J., Reuning, L., Hallenberger, M., Lüders, V., Lemmens, L., Biehl, B.C., Lewin, A., Leupold, M., Wimmers, K., Strohmenger, C.J., 2018. Dedolomitization: review and case study of uncommon mesogenetic formation conditions. Earth-Science Reviews 185, 780–805. https://doi.org/10.1016/j.earscirev.2018.07.005.

Shultz, J., Watford, D., Lehrmann, D.J., Qin, Y., Chen, X., Yu, M., Kelley, B.M., Lau, K., Payne, J.L., Minzoni, M., 2013. Triassic dolomites in carbonate platforms of south China: constraints on models for dolomitization. Geological Society of America South Central Section. 47 Annual Meeting: Abstracts with Programs, Austin, p. 24.

Song, H., Wignall, P.B., Tong, J., Song, H., Chen, J., Chu, D., Tian, L., Luo, M., Zong, K., Chen, Y., Lai, X., Zhang, K., Wang, H., 2015. Integrated Sr isotope variations and global environmental changes through the Late Permian to early Late Triassic. Earth and Planetary Science Letters 424, 140–147. https://doi.org/10.1016/j.epsl.2015.05.035.

Sun, Y., Joachimski, M.M., Wignall, P.B., Yan, C., Chen, Y., Jiang, H., Wang, L., Lai, X., 2012. Lethally hot temperatures during the Early Triassic greenhouse. Science 338, 366–370. https://doi.org/10.1126/science.1224126.

Teal, C.S., Mazzullo, S.J., Bischoff, W.D., 2000. Dolomitization of Holocene shallow-marine deposits mediated by sulfate reduction and methanogenesis in normal-salinity seawater, northern Belize. Journal of Sedimentary Research 70, 649–663. https://doi.org/10.1306/2DC4092E-0E47-11D7-8643000102C1865D.

Tong, J., Zuo, J., Chen, Z., 2007. Early Triassic carbon isotope excursions from South China: proxies for devastation and restoration of marine ecosystems following the end-Permian mass extinction. Geological Journal 42, 371–389. https://doi.org/10.1002/gj.

Vahrenkamp, V.C., Swart, P.K., 1990. New distribution coefficient for the incorporation of strontium into dolomite and its implications for the formation of ancient dolomites. Geology 18, 387–391. https://doi.org/10.1130/0091-7613(1990)018<0387:NDCFTI>2.3.CO;2.

Vasconcelos, C., Mckenzie, J.A., 1997. Microbial mediation of modern dolomite precipitation and diagenesis under anoxic conditions (Lagoa Vermelha, Rio De Janeiro, Brazil). Journal of Sedimentary Research 67, 378–390. https://doi.org/10.1306/D4268577-2B26-11D7-8648000102C1865D.

Veizer, J., Ala, D., Azmy, K., Bruckschen, P., Buhl, D., Bruhn, F., Carden, G., Diener, A., Ebneth, S., Godderis, Y., Jasper, T., Korte, C., Pawellek, F., Podlaha, O., Strauss, H., 1999. $^{87}Sr/^{86}Sr$, $\delta^{13}C$ and $\delta^{18}O$ evolution of Phanerozoic seawater. Chemical Geology 161, 59–88. https://doi.org/10.1016/S0009-2541(99)00081-9.

Wahlman, G.P., 2010. Reflux dolomite crystal size variation in cyclic inner ramp reservoir facies, Bromide Formation (Ordovician), Arkoma basin, southeastern Oklahoma. The Sedimentary Record 8, 4–9. https://doi.org/10.2110/sedred.2010.3.4.

Wang, G., Li, P., Hao, F., Zou, H., Yu, X., 2015. Origin of dolomite in the third member of Feixianguan Formation (Lower Triassic) in the Jiannan area, Sichuan Basin, China. Marine and Petroleum Geology 63, 127–141. https://doi.org/10.1016/j.marpetgeo.2015.01.019.

Wang, M., Zhang, X., Pi, D., Guo, X., 2016. Zircon U–Pb dating of Pubei granite and strontium isotope from sphalerite of the Xinhua Pb–Zn–(Ag) deposit, Yunkai Area of Guangxi Province, South China. Acta Geochimica 35, 156–171. https://doi.org/10.1007/s11631-015-0084-0.

Wang, R., Jones, B., Yu, K., 2019. Island dolostones: Genesis by time-transgressive or event dolomitization. Sedimentary Geology 390, 15–30. https://doi.org/10.1016/j.sedgeo.2019.07.002.

Warren, J., 2000. Dolomite: occurrence, evolution and economically important associations. Earth-Science Reviews 52, 1–81. https://doi.org/10.1016/S0012-8252(00)00022-2.

Whitaker, F.F., Xiao, Y., 2010. Reactive transport modeling of early burial dolomitization of carbonate platforms by geothermal convection. AAPG Bulletin 94, 889–917. https://doi.org/10.1306/12090909075.

Whitaker, F.F., Smart, P.L., Vahrenkamp, V.C., Nicholson, H., Wogelius, R.A., 1994. Dolomitization by near-normal seawater? Field evidence from the Bahamas. In: Purser, B., Tucker, M.E., Zenger, D. (Eds.), Dolomites: A Volume in Honour of

Dolomieu. vol. 21. IAS Special Publication, pp. 111–132. https://doi.org/10.1002/9781444304077.ch8.
Wilkinson, J.J., 2017. Metastable freezing: a new method for the estimation of salinity in aqueous fluid inclusions. Economic Geology 112, 185–193. https://doi.org/10.2113/econgeo.112.1.185.
Yang, Q., Liu, W., Zhang, J., Wang, J., Zhang, X., 2019. Formation of Pb–Zn deposits in the Sichuan–Yunnan–Guizhou triangle linked to the Youjiang foreland basin: evidence from Rb–Sr age and in situ sulfur isotope analysis of the Maoping Pb–Zn deposit in northeastern Yunnan Province, southeast China. Ore Geology Reviews 107, 780–800. https://doi.org/10.1016/j.oregeorev.2019.03.022.
Zhang, Y., Wang, Y., 2019. Early Neoproterozoic continental arc system at the central Jiangnan Orogen, South China: geochronological and geochemical constraints on the key igneous rock-association. Geological Society of America Bulletin 132, 638–654. https://doi.org/10.1130/B35221.1.